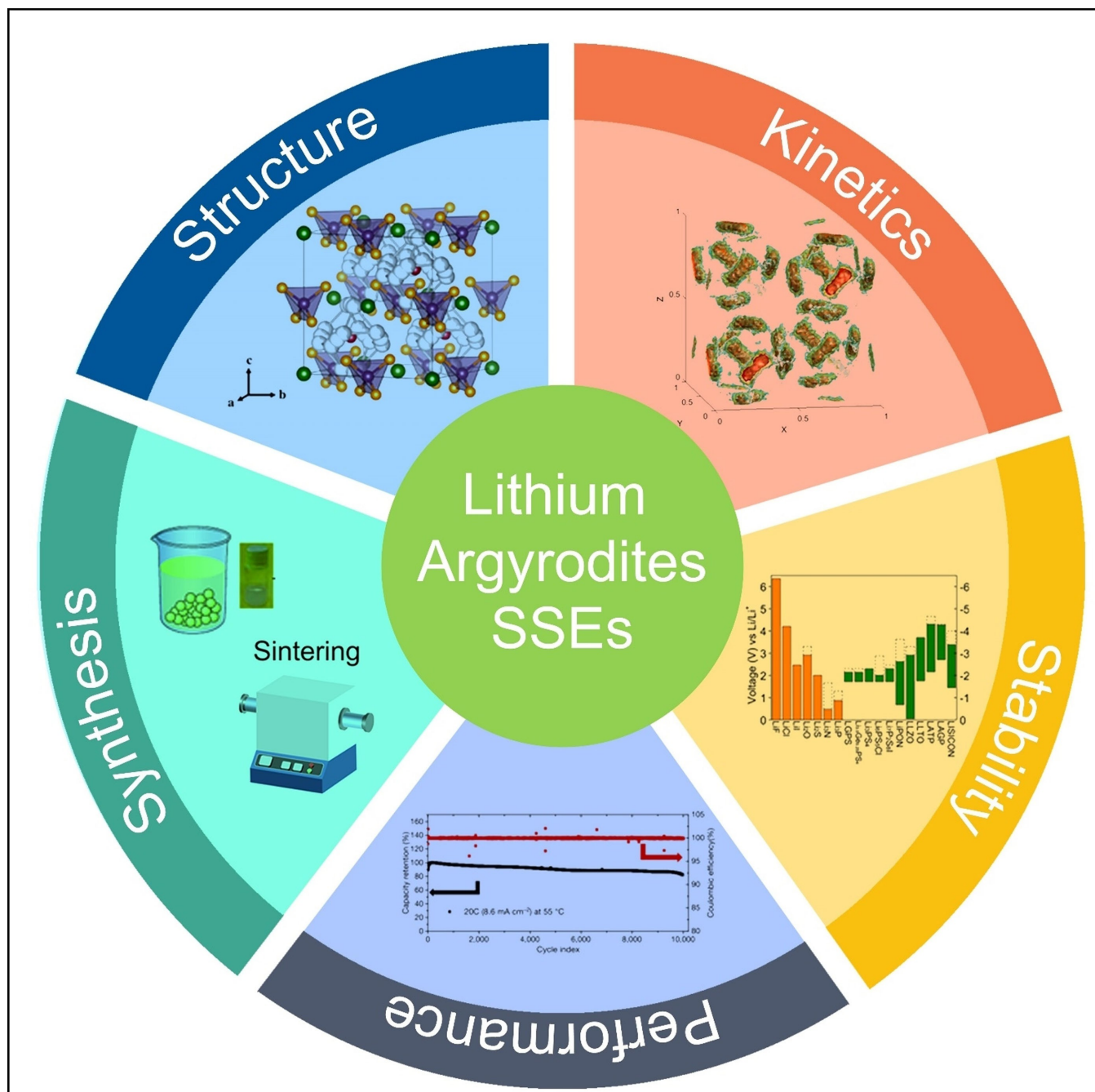


# Designing Lithium Argyrodite Solid-State Electrolytes for High-Performance All-Solid-State Lithium Batteries

Chongxing Li,<sup>[a]</sup> Shuxian Zhang,<sup>[a]</sup> Xianguang Miao,<sup>[a]</sup> Cong Wang,<sup>[a]</sup> Chengxiang Wang,<sup>[a]</sup> Zhiwei Zhang,<sup>[a]</sup> Ruta Wang,<sup>\*[a, b]</sup> and Longwei Yin<sup>\*[a]</sup>



All-solid-state lithium batteries (ASSLBs) with desirable advantages, such as high safety and energy density, simple packaging, and wide temperature tolerance, are considered promising energy storage devices to replace traditional lithium-ion batteries with organic liquid electrolytes. Solid-state electrolytes (SSEs) are the critical component in ASSLBs. Argyrodites, as a typical class of sulfide-based lithium-ion superconductors, represent the most promising SSEs with respect to their high ionic conductivity at room temperature, low cost, good compatibility towards Li metal, and extraordinary performance reported in ASSLBs. However, lithium argyrodites are inert gas-

protective, moisture-sensitive, interface-unstable, and working potential window-limited, presenting the main challenges for their commercial use. In this review, we comprehensively summarized the basic physical and chemical properties, material synthesized strategies, chemical or electrochemical stabilities, and interface engineering of lithium argyrodite SSEs. Furthermore, the recent achievements and critical challenges for lithium argyrodite from the material level to battery applications are overviewed, and the future development opportunities of integrating the lithium argyrodite SSEs into ASSLBs have been prospected.

## 1. Introduction

Lithium-ion batteries (LIBs) are widely used in the fields of electric vehicles, electronic goods, power backups, electric mobility, etc. because of their merits of high energy density, low self-discharge, long cycle life, and no memory effect.<sup>[1]</sup> The working mechanism of LIBs arises from the movement of  $\text{Li}^+$  ions between the anode and cathode materials that are usually intercalation compounds (typically graphite and  $\text{LiCoO}_2$  in the first generation of LIBs fabricated by Sony Corporation) having the ability to host  $\text{Li}^+$  ions.<sup>[2]</sup> To keep the effective transfer of  $\text{Li}^+$  ions between anode and cathode, the liquid electrolyte of  $\text{LiPF}_6$  in an organic solvent such as ethers and carbonate esters is widely used in LIBs. The flammability of organic solvent and hazards of electrolytes leakage, however, would lead to potential safety problems on LIBs.<sup>[3]</sup> Currently, there is a common agreement that the applications of SSEs by taking the place of liquid electrolytes in the LIBs could solve safety concerns effectively. The main reason is because of that non-flammable SSEs can work as a physical separation barrier on two electrodes and eliminate the leakage of electrolyte.<sup>[4]</sup>

At present, the reported SSEs for LIBs can be mainly divided into two types: polymeric and inorganic materials.<sup>[5]</sup> Polymeric SSEs mainly composed of organic polymers, lithium salts, and/or inorganic fillers. The most common example of polymeric SSEs is polyethylene oxide (PEO)-based complexes. In addition, poly(acrylonitrile) (PAN), poly(methyl methacrylate) (PMMA) and poly(vinylidene fluoride) (PVDF) based polymeric SSEs have also been exploited.<sup>[6]</sup> Polymeric SSEs have the advantages of excellent contact with electrode materials and good film-forming properties, however, suffering from low ionic conductivity at room temperature, low ionic transference number

( $<0.5$ ), and instability of the electrode/electrolyte interface. Since the 1950s, the first inorganic SSE- $\text{Li}_3\text{N}$  with high ionic conductivity of  $10^{-3}\text{ Scm}^{-1}$  at room temperature was discovered, various inorganic SSEs have been exploited for LIBs, such as perovskite-type, sodium superionic conductor (NASICON)-type, garnet-type, and sulfide-type materials.<sup>[7]</sup> These inorganic SSEs generally show considerable ionic conductivity, high ionic transference number, good thermal stability, and robust mechanical properties, shown in Figure 1. Significantly, sulfide-type SSEs (such as argyrodites, thio-LISICON, and the  $\text{Li}_{10}\text{MP}_2\text{S}_{12}$  ( $\text{M}=\text{Si}, \text{Ge}, \text{Sn}$ )) exhibit high values of lithium-ion conductivities up to  $10^{-2}\text{ Scm}^{-1}$  at room temperature, comparable to that of liquid electrolytes, such as ethylene carbonate/dimethyl carbonate with  $\text{LiPF}_6$  salt.<sup>[8]</sup>

Among sulfide-type SSEs, lithium argyrodite  $\text{Li}_6\text{PS}_5\text{X}$  ( $\text{X}=\text{Cl}, \text{Br}, \text{I}$ ) are a promising candidate for ASSLB applications because they possess high ionic conductivities originating from their unique chalcogenide structures, an effective interface between solids during operating, the advantage of utilizing cheap precursors and scalable methods for their synthesis.<sup>[9]</sup> Since the first  $\text{Li}_6\text{PS}_5\text{X}$  was synthesized in 2008, we have witnessed an astounding increase in publications regarding argyrodites, especially in the recent 5 years, as shown in Figure 2. The composition and structure, synthesis strategies and modifications, degradation mechanisms, and the stability of lithium argyrodite SSEs, have been extensively reported, as summarized in Figure 3. Notably, Samsung Electronics Co., Ltd. reported that high-performance ASSLBs with an argyrodite SSE are enabled by an Ag-C composite anode with no excess Li and a high-Ni layered oxide cathode in 2020.<sup>[10]</sup> This argyrodite SSE-based ASSLB exhibited a high energy density exceeding  $900\text{ Wh L}^{-1}$ , stable coulombic efficiency over 99.8%, and long cycle life (1,000 times), which is highly comparable to liquid electrolyte based LIBs. In 2021, Li's groups from Harvard University proposed a sulfide-type SSEs based multilayer design ( $\text{Li}_{5.5}\text{PS}_{4.5}\text{Cl}_{1.5}/\text{Li}_{10}\text{Ge}_1\text{P}_2\text{S}_{12}/\text{Li}_{5.5}\text{PS}_{4.5}\text{Cl}_{1.5}$ ) to solve the lithium dendrite growth issues, which is based on a mechanism analogous to the expansion screw effect.<sup>[11]</sup> This multilayer SSE-based ASSLB yielded extremely high cycling stability reported so far, for example, with an 82% capacity retention after 10,000 cycles at a 20 C rate and 81.3% capacity retention after 2,000 cycles at a 1.5 C rate, which is highly comparable to LIBs based liquid electrolytes.<sup>[11]</sup> These achievements demonstrate that lithium

[a] C. Li, S. Zhang, Dr. X. Miao, C. Wang, Dr. C. Wang, Dr. Z. Zhang, Prof. R. Wang, Prof. L. Yin  
Key Laboratory for Liquid-Solid Structural Evolution and Processing of Materials  
Ministry of Education, School of Materials Science and Engineering  
Shandong University  
Jinan 250061, China  
E-mail: rtwang@sdu.edu.cn  
yinlw@sdu.edu.cn  
[b] Prof. R. Wang  
Suzhou Institute of Shandong University  
Suzhou 215123, China

argyrodite SSEs are the optimal choice toward promoting the commercialization of ASSLBs. Therefore, it is significant to review the development of lithium argyrodite SSEs and batteries, summarize their challenges and opportunities, and provide a perspective for the future development of SSEs and ASSLBs.

In this review, we summarize the basic properties of lithium argyrodite SSEs, including the structure, ion conduction mechanism, and ionic conductivity of lithium argyrodite. The effect of different synthesis methods of lithium argyrodite type SSEs on Li<sup>+</sup> ionic conductivity and other properties are discussed. The chemical and electrochemical stability of lithium

argyrodite type SSEs, mainly focusing on the stability with different types of anode and cathode materials and in the air or liquid electrolytes, is later highlighted. The interface problems created by lithium argyrodite SSEs and strategies and corresponding characterization techniques to solve interface challenges are comprehensively summarized. In addition, the different applications of lithium argyrodite as composite electrolytes and SSEs are described in sequence. Lastly, the advantages and disadvantages of lithium argyrodite and its future development opportunities are also discussed.



Chongxing Li received his BS degree from the Department of Inorganic nonmetallic materials Engineering, Shandong University of Science and Technology, China in 2019. He is currently pursuing her MSc degree at the School of Materials Science and Engineering at Shandong University(SDU) under the supervision of Prof. Rutao Wang. His current research is focused on developing Li-argyrodites for all-solid-state lithium batteries.



Shuxian Zhang received his BS degree from the Agricultural Building Environment and Energy Engineering, Northeast Agricultural University, China in 2020. He is currently a PhD Candidate at the School of Materials Science and Engineering at SDU under the Prof. Rutao Wang. His current research is focused on developing Li-argyrodites for all-solid-state lithium batteries.



Xianguang Miao received his BS degree from the Department of Material Physics, Shandong University, China in 2016. He is currently a PhD candidate at the School of Materials Science and Engineering at SDU under the supervision of Prof. Longwei Yin. His current research mainly focuses on the material and structure design of solid-state lithium/sodium batteries.



Cong Wang is an undergraduate of the School of Materials Science and Engineering, Shandong University. She joined Professor Rutao Wang's research group in 2020. Her current research is focused on design of all solid-state lithium sulfur battery based on Li<sub>6</sub>PS<sub>5</sub>Cl electrolyte.



Chengxiang Wang received her PhD degrees from the Department of Material Chemistry, Shandong University (SDU), China, in 2010, under the supervision of Prof. Longwei Yin. During 2011–2014, he joined Professor Sasaki Takayoshi's group as a Research Fellow in International Center for Materials Nanoarchitectonics, National Institute for Materials Science. Later, he worked at the Institute of Materials Physics & Chemistry, SDU. His current research mainly focuses on the design and development of two-dimensional layered materials and applications of Li-ion batteries.



Zhiwei Zhang received her BS and PhD degrees from the Department of Material Chemistry, Shandong University (SDU), China, in 2012 and 2017, respectively, under the supervision of Prof. Longwei Yin. Later, she worked at the Institute of Materials Physics & Chemistry, SDU. Her current research mainly focuses on the design and development of nanostructured gel and applications of Li-ion, Na-ion, Li-S, and Li-air batteries.



Rutao Wang is a Professor of the School of Materials Science and Engineering, Shandong University. He received his Ph.D. degree in Materials Science from Lanzhou Institute of Chemical Physics, Chinese Academy of Sciences (2015). During 2015–2018, he joined the Professor Li Zhang's group as a Research Fellow in Department of Mechanical and Automation Engineering, The Chinese University of Hong Kong. Now, his research focuses on developing advanced materials for supercapacitor and all-solid-state battery.



Longwei Yin is a distinguished professor and Director of the Institute of Materials Physics & Chemistry, Shandong University (SDU), China. He received his PhD in 2001 from SDU. He completed his postdoctoral research from 2003 to 2006 at Prof. Bando Yoshiro's group at National Institute for Materials Science, Japan. He won the National Science Fund for Distinguished Young Scholars in 2010. His research interests mainly focus on energy conversion and storage devices, including Li- or Na-based secondary batteries, supercapacitors, photo/electrocatalysis, and solar cells.

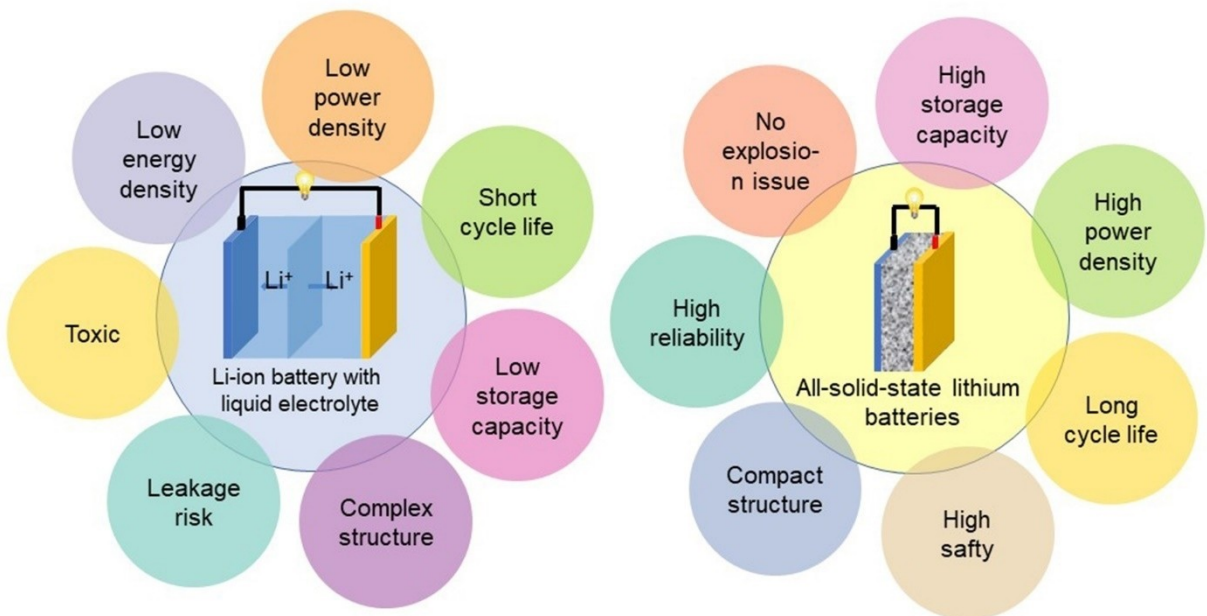


**Figure 1.** Performance comparison between LIBs using liquid electrolytes (left) and ASSLBs (right).

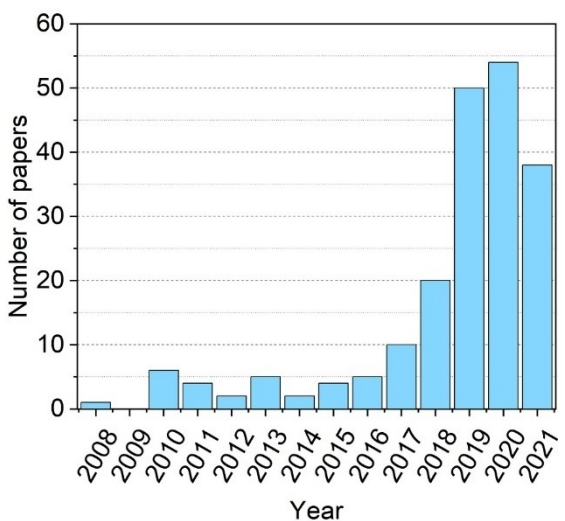


**Figure 2.** The number of papers on Argyrodite has been published since 2008 (Accessed August 25, 2021, Web of Science.)

## 2. Fundamentals of Argyrodite-Type SSEs

### 2.1. Structure of Argyrodite-Type SSEs

Lithium argyrodite, for the first time, was found by Deiseroth and co-workers in 2008.<sup>[12]</sup> The crystal structure of lithium argyrodite is analogous to the archetypal mineral argyrodite ( $\text{Ag}_8\text{GeS}_6$ ) (Figure 4).<sup>[13]</sup> The silver ions of the mineral argyrodite ( $\text{Ag}_8\text{GeS}_6$ ) can be replaced by other cations. Besides, P substituting Ge also does not change the crystal structure of argyrodites. Hence, lithium argyrodite can be obtained by replacing Ag and Ge in  $\text{Ag}_8\text{GeS}_6$  with Li and P. Li<sup>+</sup> ions can move freely in the argyrodite structure. Therefore, a high

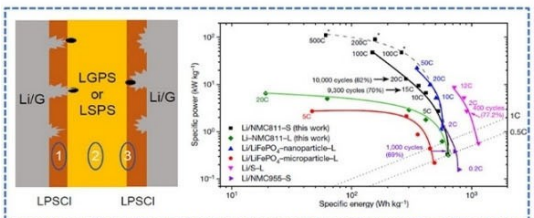
conductivity value of more than  $10^{-3} \text{ S cm}^{-1}$  can be achieved for lithium argyrodite.

### 2.2. Li-Ion Conduction Mechanism in Lithium Argyrodite SSEs

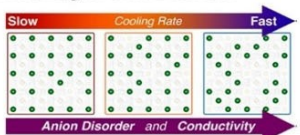
NMR is a powerful tool to detect lithium-ion transport pathways and proton exchange mechanisms due to <sup>7</sup>Li and <sup>6</sup>Li are active isotopes of NMR.<sup>[14]</sup> Compared with four-probe conductivity tests, NMR can exclude the influence of electron conductance, making the results more accurate.<sup>[15]</sup> More interesting, lithium argyrodite powder can be studied without any post-treatment while just seal it inside the ampoule to protect against moisture. To obtain deep insights into the atomicity of Li<sup>+</sup> mobility, Pecher et al. used NMR measurements to study the short-range mobility of the Li<sup>+</sup> ions in  $\text{Li}_{7-x}\text{PS}_{6-x}\text{I}_x$  ( $0 \leq x \leq 1$ ).<sup>[16]</sup> The results showed that ionic mobility is observed even at low temperature, though below 177 K the displacement of Li<sup>+</sup> is confined to about 1.5 Å. This "local mobility" reflects the fluctuation of trigonal planar coordinated sites (type 5a) (Figure 5), which is the minimum energy configuration. For larger displacements, Li<sup>+</sup> ions must pass beyond the two S<sub>3</sub>I tetrahedra. Therefore, for easy Li<sup>+</sup> conductivity, a series of interstitial sites must be reached. These sites are disfavored by 0.14 and 0.27 eV, respectively. Both interstitial sites are essential to forming a connective Li<sup>+</sup> pathway throughout the unit cell, and the configuration of higher energy accounts for the activation barrier to ionic conductivity.<sup>[16]</sup> With the temperature increased, a continuous three-dimensional diffusion pathway can only be formed if the center of the type 2 tetrahedra is included.<sup>[17]</sup>

The ionic conductivity values can be converted from the jump rates derived from spin–lattice relaxation (SLR) NMR in

Ye *et al.*(2021) –A dynamic stability design strategy for lithium metal solid state batteries

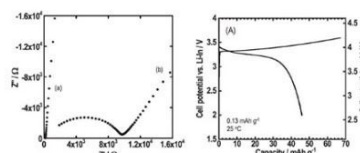


Gautam *et al.*(2019) –Rapid Crystallization and Kinetic Freezing of Site-Disorder



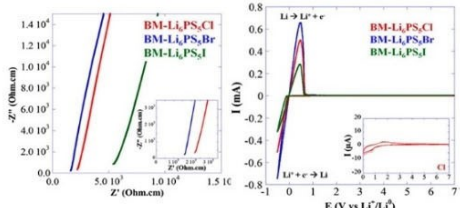
Kraft *et al.*(2017) –Influence of Lattice Polarizability on the Ionic Conductivity in Argyrodites

Yubuchi *et al.*(2015) –Preparation of Li<sub>6</sub>PS<sub>5</sub>Cl from ethanol solution



Chen *et al.*(2014) -High capacity all-solid-state Cu–Li<sub>2</sub>S/Li<sub>6</sub>PS<sub>5</sub>Br/In batteries

Boulineau *et al.*(2012) -Effect of a mechanical milling step on electrochemical performance



Kong *et al.*(2010) -The first Lithium-Oxide-Arnyrodites

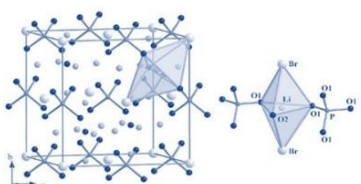
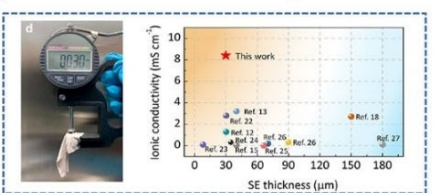
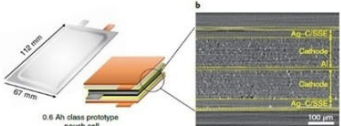


**Figure 3.** Historical development of argyrodites. [Ye *et al.* (2021)] Reproduced from Ref. [11] with permission. Copyright (2021) The Author(s), under exclusive licence to Springer Nature Limited. [Zhang *et al.* (2021)] Reproduced from Ref. [105] with permission. Copyright (2021) American Chemical Society. [Lee *et al.* (2020)] Reproduced from Ref. [10] with permission. Copyright (2020) The Author(s), under exclusive licence to Springer Nature Limited. [Gautam *et al.* (2019)] Reproduced from Ref. [61] with permission. Copyright (2019) American Chemical Society. [Minafra *et al.* (2018)] Reproduced from Ref. [33a] with permission. Copyright (2018) Royal Society of Chemistry. [Klerk *et al.* (2016)] Reproduced from Ref. [23] with permission. Copyright (2016) American Chemical Society. [Yubuchi *et al.* (2015)] Reproduced from Ref. [62] with permission. Copyright (2015) Elsevier B.V. [Boulineau *et al.* (2012)] Reproduced from Ref. [45] with permission. Copyright (2013) Elsevier B.V. [Deisereth *et al.* (2011)] Reproduced from Ref. [17] with permission. Copyright (2011) Wiley-VCH. [Kong *et al.* (2010)] Reproduced from Ref. [110] with permission. Copyright (2010) Wiley-VCH. [Deisereth *et al.* (2008)] Reproduced from Ref. [12] with permission. Copyright (2021) Wiley-VCH.

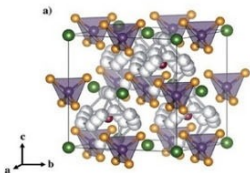
Zhang *et al.*(2021) –Flexible Sulfide Electrolyte Thin Membrane with Ultrahigh Ionic Conductivity



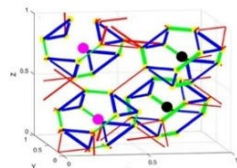
Lee *et al.*(2020) –High-energy long-cycling all-solid-state lithium metal batteries



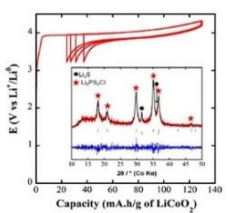
Minafra *et al.*(2018) –Effect of Si substitution



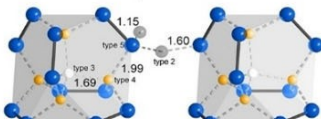
Klerk *et al.*(2016) –Diffusion Mechanism of Li Argyrodite



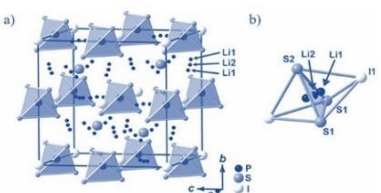
Boulineau *et al.*(2013) –Performance of all-solid-state batteries using Li<sub>6</sub>PS<sub>5</sub>Cl as solid electrolyte



Deisereth *et al.*(2011) –Possible Three-dimensional Diffusion Pathways for Lithium Ions



Deisereth *et al.*(2008) -First time synthesis of Li<sub>6</sub>PS<sub>5</sub>X



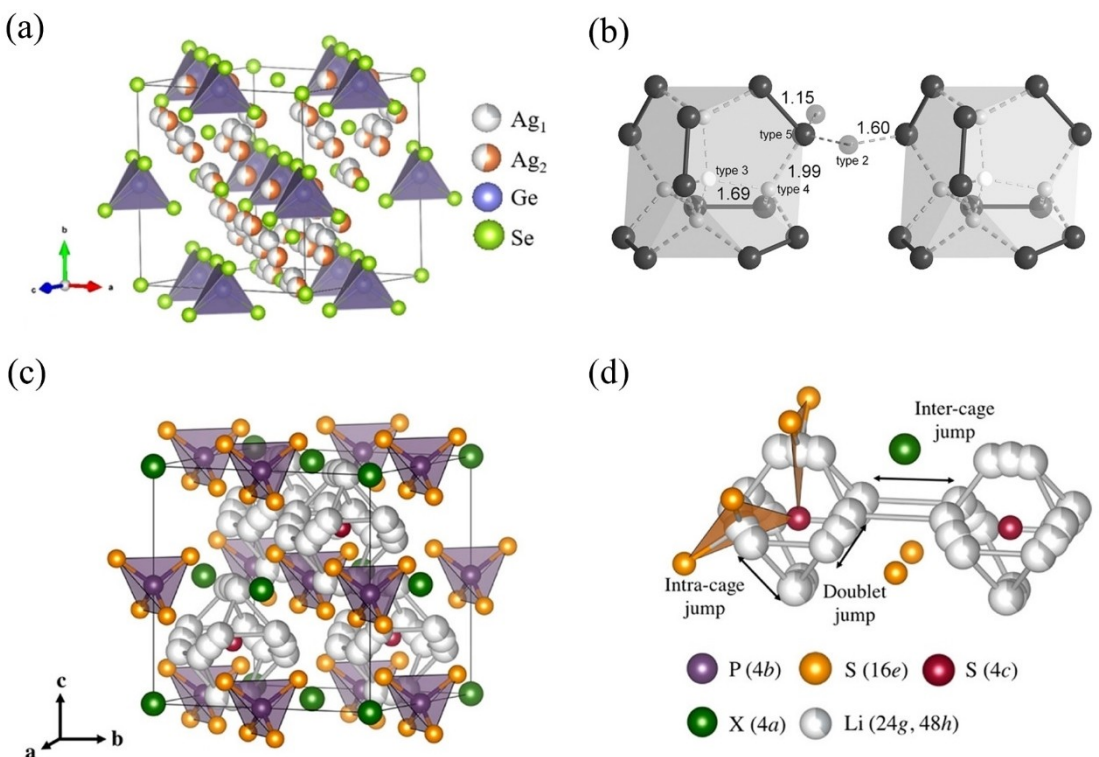


**Figure 4.** a) Cubic crystal structure of  $\text{Ag}_8\text{GeSe}_6$  at 473 K. Reproduced from Ref. [110] with permission. Copyright (2011) Wiley-VCH. b) Two local diffusion pathways of  $\text{Li}^+$  ions in  $\text{HT-Li}_6\text{PS}_5\text{I}$ . Reproduced from Ref. [17] with permission. Copyright (2019) American Chemical Society. c) Crystal structures of  $\text{Li}_6\text{PS}_5\text{X}$  with  $\text{X}=\text{Cl}, \text{Br}, \text{I}$ . In the ordered structure,  $\text{X}^-$  anions form a cubic close-packed lattice with  $\text{PS}_4^{3-}$  tetrahedra in the octahedral sites and the free  $\text{S}^{2-}$  (Wyckoff 4c) in half of the tetrahedral holes. d) The free  $\text{S}^{2-}$  anions and the corner of the  $\text{PS}_4^{3-}$  tetrahedra form Frank-Kasper polyhedra, which enclose two different  $\text{Li}$  positions. The  $\text{Li}$  positions form localized cages in which multiple jump processes are possible. Jumps between the lithium positions (48 h-24 g-48 h, doublet jump), intracage jumps (48 h-48 h), and intercage jumps can occur. Reproduced from Ref. [111] with permission. Copyright (2017) American Chemical Society.

view of the Einstein-Smoluchowski equation and the Nernst-Einstein equation.<sup>[18]</sup> The results of SLR NMR analysis showed that the ionic conductivity of lithium argyrodite was strongly related to the disordered distribution of anions.<sup>[18]</sup> For  $\text{Li}_6\text{PS}_5\text{I}$ , the inter-cage transition process that determines the long-distance migration of  $\text{Li}^+$  has much larger activation energy than compounds  $\text{X}=\text{Br}$  and  $\text{X}=\text{Cl}$ , due to the ordered distribution of  $\text{I}^-$  and  $\text{S}^{2-}$ .<sup>[19]</sup> In  $\text{Li}_6\text{PS}_5\text{Br}$ , an optimal balance between lattice properties (including polarizability) and dislocation is established, resulting in rapid rotation skips and easily translational  $\text{Li}^+$  displacements. For  $\text{Li}_6\text{PS}_5\text{Cl}$ , the small lattice constant and the intense ion position disorder result in a relatively high jump rate. Anion substitution can affect the lattice parameters, lattice softness, and Li bond of  $\text{Li}_6\text{PS}_5\text{X}$ , to some extent, which is beneficial to the translation mechanics of  $\text{Li}^+$  but is detrimental to the fast-rotating ion kinetics.<sup>[20]</sup> The formation energy of antisite defects is proportional to the radius of the halogen atom. For example, the ionic radius of iodine is the largest among the halogen atoms, resulting in the highest degree of order and the lowest ionic conductivity of  $\text{Li}_6\text{PS}_5\text{X}$ .<sup>[21]</sup>

Figure 6 shows the high mobility of  $\text{Li}^+$  in  $\text{Li}_6\text{PS}_5\text{Cl}$  lattice is plotted in the narrowing of the so-called “motional” of the static  ${}^7\text{Li}$  NMR spectrum with increasing temperature.<sup>[12,22]</sup> Through the SLR NMR measurements, both short-range and long-range diffusion parameters can be obtained.<sup>[15]</sup> The low-

temperature flanks of NMR SLR  $1/T_1$  rate (characterized by the activation energy of  $0.09 \pm 0.02$  eV) represent a combination of two short-range jumps; the high-temperature side ( $0.29 \pm 0.01$  eV) represents a long-distance cage-to-cage transition, which is the cause of macro diffusion.<sup>[15,16]</sup> SLR NMR results show that a small interface region between the electrode and electrolyte phase limits the transport of Li ions at the interface. Although the exchange activation energy ( $0.12 \pm 0.01$  eV) is smaller than the bulk diffusion activation energy ( $0.29 \pm 0.01$  eV), the diffusion coefficient of exchange is small.<sup>[22]</sup> It is crucial to increase the electrolyte-electrode interface to improve the performance of ASSLBs.

Computational methods were usually used to penetrate the mechanisms of ionic mobility and conductivity in lithium argyrodite crystals. Pecher et al. simulated a series of  $\text{Li}_{7-X}\text{PS}_{6-X}\text{I}_X$  ( $0 \leq X \leq 1$ ) single crystal models by molecular dynamics (MD) method.<sup>[16]</sup> The simulated MD results show that there are two stages in the motion of  $\text{Li}^+$ , the local mobility at low temperature and the actual conductivity at high temperature. De Klerk et al. found three different types of local jumps in MD simulation between 48 h sites of HT argyrodites structure.<sup>[23]</sup> One is between the paired 48 h sites over  $1.9 \text{ \AA}$ , called doublet jumps (48 h-24 g->48 h, back-and-forth jumps). The second type is a jump between different 48 h pairs within the cage with  $2.25 \text{ \AA}$ , which is called an intracage jump (48 h-48 h). The third type is a jump in which four cages in each unit cell are

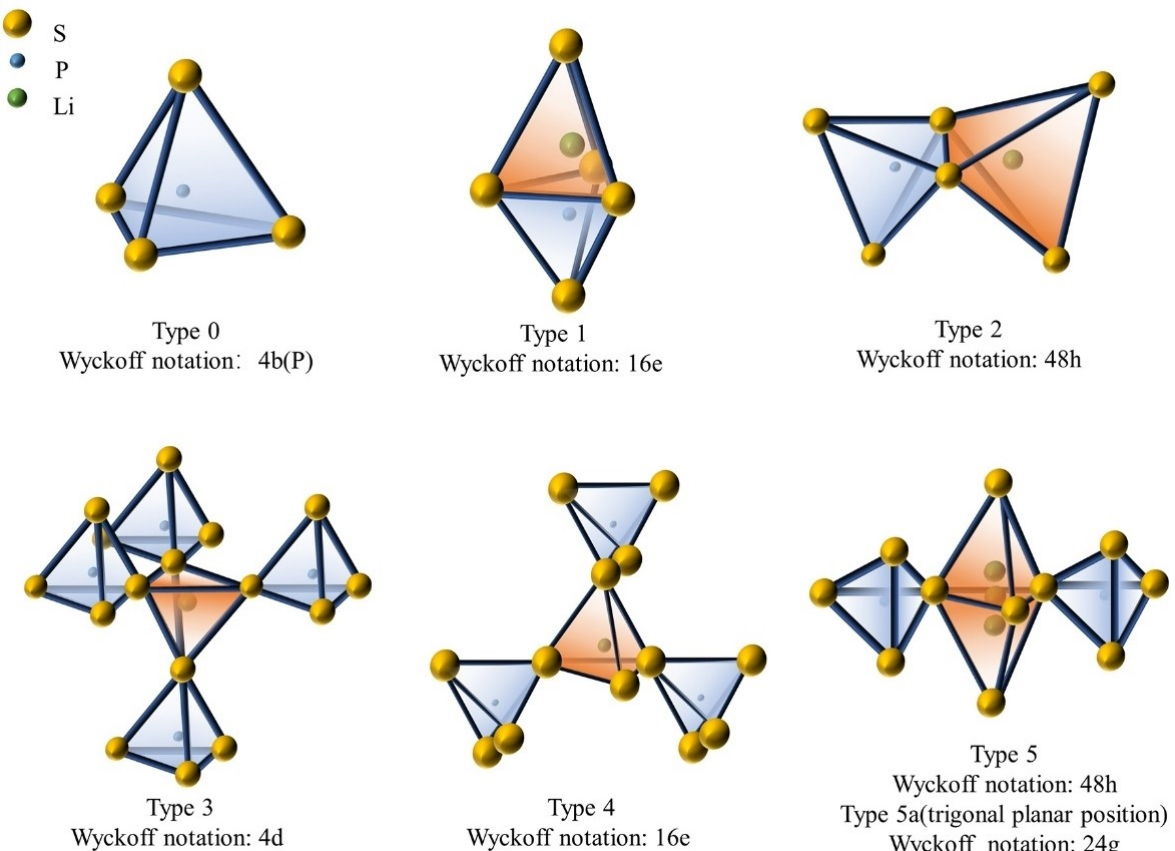


**Figure 5.** Crystal chemical analysis of the 136 tetrahedral holes formed by the S atoms in the unit cell of HT-Li<sub>3</sub>PS<sub>6</sub>. Reproduced from Ref. [112] with permission. Copyright (2010) Wiley-VCH.

connected because the distances are different, which is called intercages jumps (48 h-48 h). Doublet jumps and intracage jumps have similar activation energy with a value ranging from 0.10 to 0.17 eV (depending on temperature). The activation energy for intercage jumps is large, ranging from 0.23 to 0.25 eV (depending on temperature).<sup>[22]</sup> For the Li-ion diffusion path to penetrate the entire crystal, three types of jumps must occur. The one with the lowest jump rate limits the macro diffusion. The rate of inter-cage hopping is at least five times lower than that of other types of hopping. Although these three types of hopping are necessary for macro-diffusion, the first step to increase Li<sup>+</sup> conductivity in lithium argyrodite is to increase the rate of inter-cage hopping. Increased temperature leads to the increasement of hopping between cages, thus improving macro-diffusion.<sup>[24]</sup>

Computational methods were usually used to penetrate the mechanisms of ionic mobility and conductivity in lithium argyrodite crystals. Pecher et al. simulated a series of Li<sub>7-x</sub>PS<sub>6-x</sub> (0 ≤ X ≤ 1) single crystal models by molecular dynamics (MD) method.<sup>[16]</sup> The simulated MD results show that there are two stages in the motion of Li<sup>+</sup>, the local mobility at low temperature and the actual conductivity at high temperature. De Clerk et al. found three different types of local jumps in MD simulation between 48 h sites of HT argyrodites structure.<sup>[23]</sup> One is between the paired 48 h sites over 1.9 Å, called doublet

jumps (48 h-24 g-48 h, back-and-forth jumps). The second type is a jump between different 48 h pairs within the cage with 2.25 Å, which is called an intracage jump (48 h-48 h). The third type is a jump in which four cages in each unit cell are connected because the distances are different, which is called intercages jumps (48 h-48 h). Doublet jumps and intracage jumps have similar activation energy with a value ranging from 0.10 to 0.17 eV (depending on temperature). The activation energy for intercage jumps is large, ranging from 0.23 to 0.25 eV (depending on temperature).<sup>[22]</sup> For the Li-ion diffusion path to penetrate the entire crystal, three types of jumps must occur. The one with the lowest jump rate limits the macro diffusion. The rate of inter-cage hopping is at least five times lower than that of other types of hopping. Although these three types of hopping are necessary for macro-diffusion, the first step to increase Li<sup>+</sup> conductivity in lithium argyrodite is to increase the rate of inter-cage hopping. Increased temperature leads to the increasement of hopping between cages, thus improving macro-diffusion.<sup>[24]</sup>

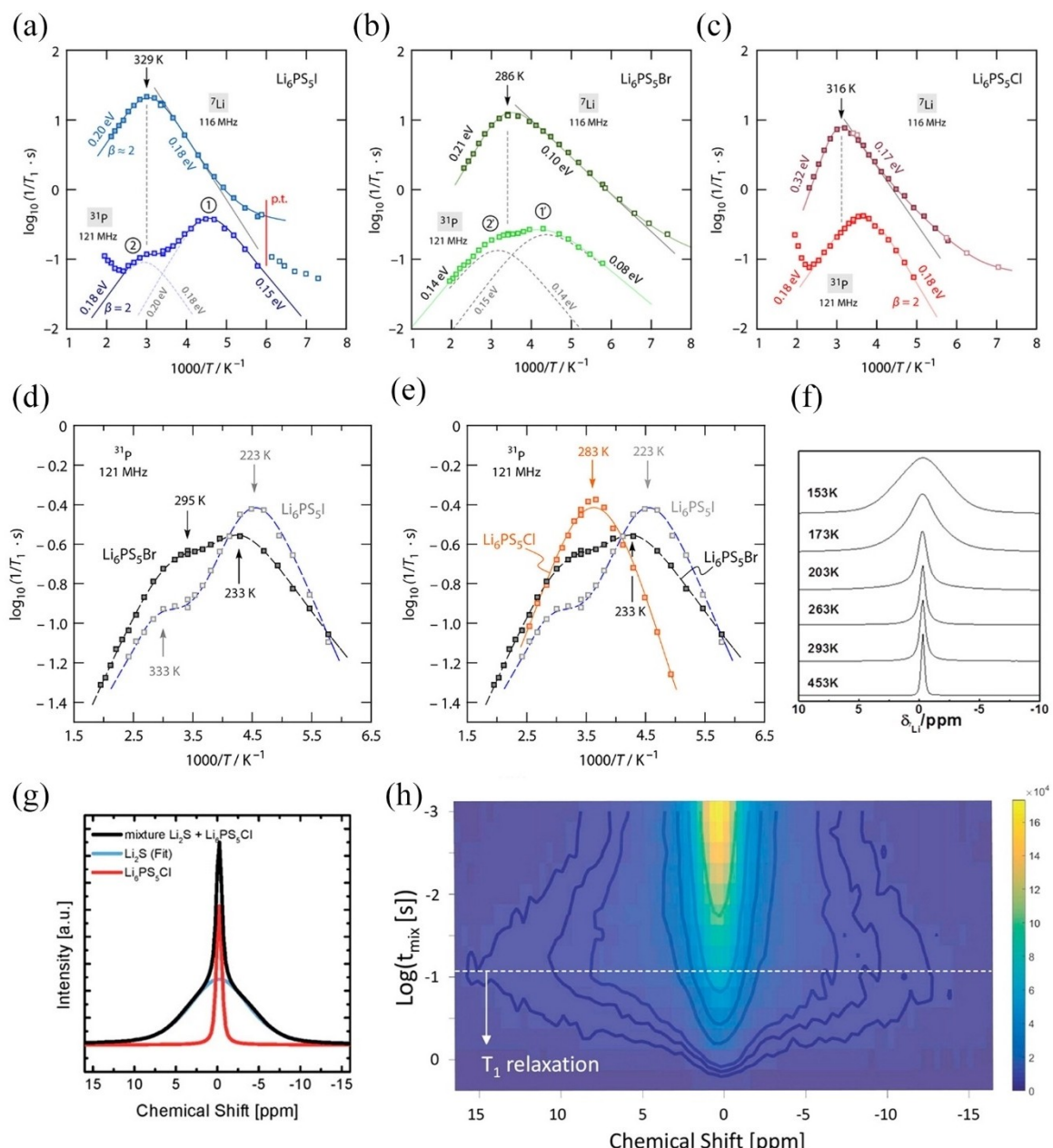


**Figure 6.** Diffusion-induced  $^7\text{Li}$  (116 MHz) and  $^{31}\text{P}$  (121 MHz) SLR NMR rates ( $\log_{10}(R_1)$  plotted vs  $1000/T$ ) of a)  $\text{Li}_6\text{PS}_5\text{I}$ , b)  $\text{Li}_6\text{PS}_5\text{Br}$ , and c)  $\text{Li}_6\text{PS}_5\text{Cl}$ .<sup>[20]</sup> d, e) Direct comparison of the  $^{31}\text{P}$  SLR NMR rate peaks  $R_1(1/T)$  seen for  $\text{Li}_6\text{PS}_5\text{I}$ ,  $\text{Li}_6\text{PS}_5\text{Br}$ , and  $\text{Li}_6\text{PS}_5\text{Cl}$ . Reproduced from Ref. [20] with permission. Copyright (2019) American Chemical Society. f) Motional narrowing curves of the static  $^7\text{Li}$  NMR resonance of  $\text{Li}_6\text{PS}_5\text{Cl}$ . g) The static  $^7\text{Li}$  NMR spectrum of the electrode-solid electrolyte  $\text{Li}_2\text{S} - \text{Li}_6\text{PS}_5\text{Cl}$  mixture. h) One-dimensional  $^7\text{Li} - ^7\text{Li}$  NMR exchange experiment probing the Li-ion transport from the electrolyte  $\text{Li}_6\text{PS}_5\text{Cl}$  phase to the electrode  $\text{Li}_2\text{S}$  phase at room temperature. Reproduced from Ref. [22] with permission. Copyright (2016) American Chemical Society.

### 2.3. Impact Factors on Ionic Conductivity of Lithium Argyrodite SSEs

Ionic conductivity is one of the most important factors for evaluating the performance of SSEs. To achieve the higher power density of ASSLBs, ionic conductivity  $\geq 10^{-3} \text{ S cm}^{-1}$  at room temperature is necessary for SSEs. Both for oxide or sulfide electrolytes, the ionic conductivity of the grain boundaries is relatively low, thus the grain size plays a greater role in ionic conductivity. Besides, the gaps between the electrolyte particles are difficult to remove completely during the synthe-

sized process, which also plays an important role in reducing the ionic conductivity. Optimizing the synthesis process, such as using isostatic pressure preparation, can largely improve the ionic conductivity of lithium argyrodite SSEs.<sup>[17]</sup> The synthesis parameters on ionic conductivity of lithium argyrodite solid-state electrolytes would be discussed in the followed Section 3 of the synthetic method. Here, we mainly focus on several important impact factors, such as the composition of argyrodites and doping or replacing.

The introduction of excessive Li can increase the occupancy of the interstitial sites, which is beneficial to improve the  $\text{Li}^+$

ions conductivity of  $\text{Li}_6\text{PS}_5\text{Cl}$ . Deng et al. predicted that the ionic conductivity of  $\text{Li}_{6.25}\text{PS}_{5.25}\text{Cl}_{0.75}$  containing excess Li at room temperature is about  $14 \text{ mS cm}^{-1}$  through ab initio molecular dynamics simulations.<sup>[25]</sup> In fact, the ionic conductivity of  $\text{Li}_6\text{PS}_5\text{Cl}$  is difficult to reach this theoretical value, which is ascribed to that the grain boundaries and impurities are difficult to be removed completely during the experimental process. Replacing  $\text{Li}^+$  with  $\text{Al}^{3+}$  can also improve the ionic conductivity of lithium argyrodite. Recent studies showed that  $\text{Al}^{3+}$  partially occupied the 24 g Wyckoff position of  $\text{Li}^+$ .<sup>[26]</sup> As the ion radius of  $\text{Al}^{3+}$  is smaller than  $\text{Li}^+$ , the lattice parameters decrease. Because  $\text{Al}^{3+}$  provides greater Coulomb repulsion, the doublet jump (48 h-24 g-48 h) becomes longer. The distance of the intracage jump and intercage jump is relatively short, which results in the increment of ionic conductivity.

We also noted that the activation energy of long-range diffusion in  $\text{Li}_6\text{PS}_5\text{X}$  largely depended on the electrostatic interaction between the divalent chalcogenide anions and  $\text{Li}^+$  ions through first-principles calculations. Replacing  $\text{S}^{2-}$  with other chalcogenide anions with lower electronegativity, such as  $\text{Se}^{2-}$ <sup>[27]</sup>,  $\text{Te}^{2-}$ <sup>[28]</sup>, leads to higher ionic conductivity and lower activation energy of  $\text{Li}_6\text{PS}_5\text{X}$ . The ionic conductivity of  $\text{Li}_6\text{PS}_{5-x}\text{Se}_x$  and  $\text{Li}_6\text{PS}_{6-x}\text{Se}_x$  increases with the increment of Se substitution.<sup>[27,29]</sup> Increasing the  $\text{Cl}^-/\text{S}^{2-}$  mole ratio also has a systematic and remarkable impact on  $\text{Li}^+$  ion diffusivity in the crystal lattice. Weakened interactions between the mobile  $\text{Li}^+$  ions and surrounding framework anions incurred by substitution of divalent  $\text{S}^{2-}$  for monovalent  $\text{Cl}^-$  is in favor of enhancing  $\text{Li}^+$  ion diffusivity, along with an increase of site disorder and a high concentration of lithium vacancy.<sup>[30]</sup> Zhou et al. demonstrated that the ionic conductivities of  $\text{Li}_{5.75}\text{PS}_{4.75}\text{Cl}_{1.25}$  and  $\text{Li}_{5.5}\text{PS}_{4.5}\text{Cl}_{1.5}$  synthesized via a liquid phase method are  $3.0 \text{ mS cm}^{-1}$  and  $3.9 \text{ mS cm}^{-1}$ , respectively.<sup>[31]</sup> Thus, the ionic conductivity largely increases with the increment of Cl/S. Although  $\text{Li}_5\text{PS}_4\text{Cl}_2$  has not yet been synthesized, ab initio nonequilibrium molecular dynamics simulations suggest that it has a very high ionic conductivity.<sup>[32]</sup> Since the degree of disorder of  $\text{S}^{2-}$  and  $\text{Br}^-$  in  $\text{Li}_6\text{PS}_5\text{Br}$  is already very high, there is no noticeable change in the degree of disorder after replacement of  $\text{S}^{2-}$ .<sup>[33]</sup>

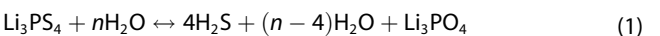
Besides, replacing P with Si will also lead to the increment of ionic conductivity for  $\text{Li}_6\text{PS}_5\text{X}$  ( $\text{X} = \text{Br}, \text{I}$ ). As we know, the ionic radius of Si is larger than P. As the Si content increases, the lattice parameter of  $\text{Li}_6\text{PS}_5\text{X}$  will increase linearly until reaching the dissolution limit. The increased lattice parameter will lead to the  $\text{Li}^+$  diffusion path becoming wide, which is conducive to the improvement of  $\text{Li}^+$  conductivity. The introduction of Si will also generate more S vacancies, thus increasing the solubility of  $\text{Li}^+$  ions in the crystal structure.<sup>[33a]</sup> In  $\text{Li}_6\text{PS}_5$ , there are no disordered sites between  $\text{S}^{2-}$  and  $\text{I}^-$ . The introduction of Si will lead to an increase in the degree of disorders, which is in favor of the improvement of ionic conductivity.<sup>[33b,34]</sup> Introducing Ge or Sn into  $\text{Li}_6\text{PS}_5$  shows the same effect with Si introduction.<sup>[33b,c,35]</sup> Similar results are observed in the case of complete substitution of P with Al or Ge.<sup>[36]</sup>

### 3. Stability of Lithium Argyrodite SSEs

#### 3.1. Stability in the Humid Air of Lithium Argyrodite SSEs

The resistance to hydrolysis is very important for the stability of lithium argyrodite SSEs. While  $\text{P}^{5+}$  has a high oxygen affinity, the sulfide electrolyte containing  $\text{PS}_4^{3-}$  will undergo a chemical reaction to produce highly toxic  $\text{H}_2\text{S}$  gas when it encounters humid air.<sup>[33e]</sup> While lithium argyrodite is highly reactive and can react immediately with water and oxygen even at the ppm level, lithium argyrodite based on LIBs needs to be assembled in a dry and oxygen-free environment, thus significantly increasing the cost.<sup>[37]</sup> Zhang et al. studied the hydrolysis resistance of  $\text{Li}_6\text{PS}_5\text{Cl}$  by exposing it to air with about 65% humidity.<sup>[38]</sup> After 10 min of exposure to air, several XRD peaks assigned to impurity can be found due to the decomposition of  $\text{Li}_6\text{PS}_5\text{Cl}$ . The authors further found a nonlinear dependence between ionic conductivity and exposure time. The value of ionic conductivity decreases from  $1.8 \text{ mS cm}^{-1}$  for the pristine sample to  $1.56$ ,  $1.43$ , and  $0.87 \text{ mS cm}^{-1}$  for air exposure for 10 min, 1 h, and 24 h, respectively. The above experimental results suggest that  $\text{Li}_6\text{PS}_5\text{Cl}$  can be exposed to air only for a short time.

In addition, Chen et al. developed a systematic method to examine the structure and hydrolytic stability of argyrodites by calculating the dissociation energy of each related critical reaction from ab initio data via the density functional method.<sup>[24a]</sup> To determine the critical reaction for hydrolysis, it is assumed that an excess of n-water molecules is available. For a  $\text{Li}-\text{P}-\text{S}-\text{H}-\text{O}$  system, the critical reaction is shown in Equation (1).



For other systems, the critical reaction is related to the type of cations. The results from theoretical calculations show that all lithium argyrodites have negative decomposition energy when they are in contact with water. Argyrodites containing phosphorus or silicon are very sensitive to water, while argyrodites containing germanium, tin, or arsenic are not easy to be hydrolyzed. Zhao et al. used Sn to replace the P element in  $\text{Li}_6\text{PS}_5\text{I}$ .<sup>[33e]</sup> And they found that the substituted Sn in the crystal lattice tended to combine with S instead of O, thus the argyrodites electrolyte has high structural stability and improved air stability. lithium argyrodite compounds without halogen atoms have lower hydrolysis stability than those with halogens. For lithium argyrodite with the same halogen contents (Such as Cl, Br, I), the hydrolysis stability decreases slightly with the increase of the atom size of halogen atoms.<sup>[24a]</sup>

To solve the inherent atmospheric and chemical instabilities in air, Jung et al. proposed a strategy that  $\text{Li}_6\text{PS}_5\text{Cl}$  SSE was coated with a thin oxysulfide nanolayer (~50 nm thick) as the protective layer via an environmental mechanical alloying (EMA) method. In this EMA method, raw materials including  $\text{LiCl}$ ,  $\text{Li}_2\text{S}$ , and  $\text{P}_2\text{S}_5$  were initially mixed and then converted into glass-ceramic argyrodites via high-energy ball milling under an inert atmosphere. Finally, oxygen gas with a high partial

pressure was introduced, then a thin oxide coating layer on argyrodites was formed. The oxysulfide coating layer was demonstrated to have high chemical stability to prevent structural degradation of the core sulfides and to increase the reliability of the powder during wet casting processes and cell operations. For example, the sulfide SE with a core-shell structure initially had an average ionic conductivity of  $3.02 \times 10^{-3} \text{ S cm}^{-1}$ , while the ionic conductivity of as-prepared argyrodites is more than  $2.5 \times 10^{-3} \text{ S cm}^{-1}$  even after air exposure (30 min, RH 35% at 25 °C). This strategy provides new possibilities for enhancing the air stability of lithium argyrodite SSEs.

Overall, many novel strategies have been proposed to improve the stability in humid air, however, effective ways are still lacking. From the point of view of applications, the stability of lithium argyrodite in humid air is still a big challenge, which is needed to be solved to reduce the processing steps and costs in the future. Especially, uncovering the structural evolution and hydrolysis mechanism of lithium argyrodite exposed in water and air may provide valuable guidance for developing new-type lithium argyrodite with anti-water/air properties for reducing the manufacturing costs of ASSLBs.

### 3.2. Stability with Anode Materials

Lithium argyrodite would be directly reacted with metal Li to form interphase (or SEI) composed of  $\text{Li}_3\text{P}$ ,  $\text{Li}_2\text{S}$ , and  $\text{LiX}$  as confirmed by XPS results. The reaction mechanism can be described as followed Equation (2):



Here  $\text{Li}_2\text{S}$ , as the main product, has very low ionic and electronic conductivities. Therefore, the as-formed SEI is highly resistive, which potentially goes against the electrochemical performance of ASSLBs. The growth rate of the SEI can be evaluated by the Wagner model [Eq. (3)]:

$$R = \frac{1}{A} \cdot \frac{(\sigma_{\text{el}})^{\frac{1}{2}}}{\sigma_{\text{ion}}} \cdot \left( \frac{2 \cdot M_{\text{SEI}} \cdot \mu_A^0}{F^2 \cdot \rho_{\text{SEI}} \cdot x} \right)^{\frac{1}{2}} (t)^{\frac{1}{2}} = k' \cdot (t)^{1/2} \quad (3)$$

From Equation 5, the variation of resistance over time is described by the parabolic rate constant  $k'$ . The theoretical results demonstrated that  $\text{Li}_6\text{PS}_5\text{Cl}$ ,  $\text{Li}_6\text{PS}_5\text{Br}$ , and  $\text{Li}_7\text{P}_3\text{S}_{11}$  exhibited a nearly similar process of sluggish SEI formation. Therefore, the approximate interphase growth rate and SEI resistance were found for  $\text{Li}_6\text{PS}_5\text{Cl}$ ,  $\text{Li}_6\text{PS}_5\text{Br}$ , and  $\text{Li}_7\text{P}_3\text{S}_{11}$ . On the contrary,  $\text{Li}_6\text{PS}_5\text{I}$  exhibited a particularly fast SEI formation rate with much higher SEI resistance.<sup>[39]</sup>

To study the Li-dendritic growth in  $\text{Li}_6\text{PS}_5\text{Cl}$  SSEs, in situ Auger electron microscopy and spectroscopy techniques were employed.<sup>[40]</sup> It has been found that volume expansion/contraction of Li metal anodes is strongly related to Li injection/extraction in the continuous charge/discharge cycles. In addition, Li migration to the Li metal anode is strongly dependent on the pressing force applied to the

sample during the charge/discharge process. As large local pressure is applied, excess Li-ions are deposited on the anode, leading to the irreversible growth of lithium metals. While the volume expansion of the Li metal anode is negligible at the unpressurized sample position, the poor capacity of the ASSLBs is observed. Therefore, homogeneous pressurization on the samples is the key factor to achieve long-term cycles for ASSLBs. Dou and co-workers studied the effects of different stack pressures on the creep of lithium metal and dendrite growth in  $\text{Li}|\text{Li}_6\text{PS}_5\text{Cl}|\text{NCA}$  batteries.<sup>[41]</sup> A suitable stack pressure improves the interface contact and reduces the resistance. When the stack pressure is too high, the dendrites will creep along the holes, resulting in short-circuited ASSLBs. The authors further demonstrated that under a low stack pressure of 5 MPa, a reliable plating and stripping for more than 1000 h in a lithium symmetric cell came true. Moreover, a  $\text{Li}|\text{Li}_6\text{PS}_5\text{Cl}|\text{LiNi}_{0.80}\text{Co}_{0.15}\text{Al}_{0.05}\text{O}_2$  ASSLB still operated more than 200 cycles at room temperature, even a plating more than 4  $\mu\text{m}$  of lithium per charge occurred.

Ionic and electronic conductivity are other important factors for lithium argyrodite. To achieve a high-power output, the minimum requirement of ionic conductivity of SSEs should be exceeded by more than  $10^{-4} \text{ S cm}^{-1}$ .<sup>[42]</sup> If the ionic conductivity is too low, it will lead to high polarization and over-potential. For lithium argyrodite, the ionic conductivity of can reach  $10^{-3} \text{ S cm}^{-1}$  at room temperature, a low polarization/over-potential is expected.<sup>[43]</sup> Besides, the high electronic conductivity of SSEs gives rise to Li dendrites during the lithium electroplating process.<sup>[3]</sup> To realize dendrite-free lithium plating at the current densities of 1 or 10  $\text{mA cm}^{-2}$ , the electronic conductivity of SSEs should be below  $10^{-10}$  or  $10^{-12} \text{ S cm}^{-1}$ . Hwang et al. demonstrated that the electronic conductivity of lithium argyrodite is close to  $3 \times 10^{-8} \text{ S cm}^{-1}$ , which is higher than the threshold value of dendrite-free lithium.<sup>[44]</sup> As a result, Li dendrites formed on lithium argyrodite are inevitable. Further studies on reducing the electronic conductivity of lithium argyrodite should be carried out.

The structural stability of SSEs is also strongly related to the electrochemical window of lithium argyrodite. Boulaineau et al. design a stainless steel/BM- $\text{Li}_6\text{PS}_5\text{X}/\text{Li}$  cell to evaluate the electrochemical stability of  $\text{Li}_6\text{PS}_5\text{X}$  ( $\text{X} = \text{Cl}, \text{Br}, \text{I}$ ) from CV curves.<sup>[45]</sup> The scan rate of CV was 1  $\text{mV s}^{-1}$  with an operating potential window ranging from -0.5 to +7 V. From CV curves, the cathodic and anodic peaks are close to 0 V, corresponding to the reduction deposition ( $\text{Li}^+ + e^- \rightarrow \text{Li}$ ) and stripping ( $\text{Li} \rightarrow \text{Li}^+ + e^-$ ) of lithium metal, respectively. Especially, amplifying the curve of chloride phase to microampere level, no other electrochemical reaction was found in five cycles. However, this work may not provide enough evidence to prove  $\text{Li}_6\text{PS}_5\text{X}$  ( $\text{X} = \text{Cl}, \text{Br}, \text{I}$ ) SSEs with a wide operating window, especially in a practical use where conductive carbon would be mixed with  $\text{Li}_6\text{PS}_5\text{X}$  ( $\text{X} = \text{Cl}, \text{Br}, \text{I}$ ) SSEs and active electrode materials to compact into an electrode. If the SS was replaced by SE + carbon mixture, the SE will show a significant anodic decomposition peak around 3 V (vs.  $\text{Li}/\text{Li}^+$ ).<sup>[46]</sup> Additionally, more theoretical calculations of thermodynamics also show that sulfide electrolytes have a narrow electrochemical window, as

shown in Figure 7(a and b).<sup>[47]</sup> There are two reasons for the wide electrochemical window observed from the CV test. One is that the kinetic stability is caused by the slow decomposition reaction and the low electronic conductivity at the interface.<sup>[47b,c,48]</sup> The other is that on account of the high ionic conductivity of the SSEs, the kinetics of (de)lithiation is dominant compared with direct decomposition. For example, Li<sub>6</sub>PS<sub>5</sub>Cl generates Li<sub>4</sub>PS<sub>5</sub>Cl and Li<sub>11</sub>PS<sub>5</sub>Cl during initial oxidation and reduction, and then gradually decomposes into final products, such as S and P<sub>2</sub>S<sub>7</sub><sup>4-</sup> or Li<sub>3</sub>P (Figure 7c and d). This phase change of Li<sub>6</sub>PS<sub>5</sub>Cl is also demonstrated by various electrochemical and structural characterizations including differential capacitance curves ( $dQ/dV$ ), XRD, and NMR-*YT*41. In this case, the  $dQ/dV$  curves obtained by slow charging and discharging appear more accurately than CV tests.<sup>[47a]</sup>

At present, the optimal anodic candidate for lithium argyrodite SSEs is Li-In alloy which can be ascribed to the relatively good reversibility and recyclability of Li-In alloy. However, the large volume change of Li-In during the cycles leads to poor interface contact and the increased interface resistance. Some studies proposed that  $\text{Li}_4\text{Ti}_5\text{O}_{12}$  (LTO) was an optimal anode material for lithium argyrodite-based ASSLBs.<sup>[49]</sup> This is because that LTO has good compatibility with  $\text{Li}_6\text{PS}_5\text{Cl}$  during the cycles and does not produce chemical or electrochemical degradation. However, the high  $\text{Li}^+$  insertion/desorption potential of  $\sim 1.55$  V (vs.  $\text{Li}/\text{Li}^+$ ) of LTO renders the low working potential, thus limiting the energy density of ASSLBs. Consequently, more systematic studies are required to fully understand the stability of lithium argyrodite with anode materials. Additionally, new electrode materials or interface and

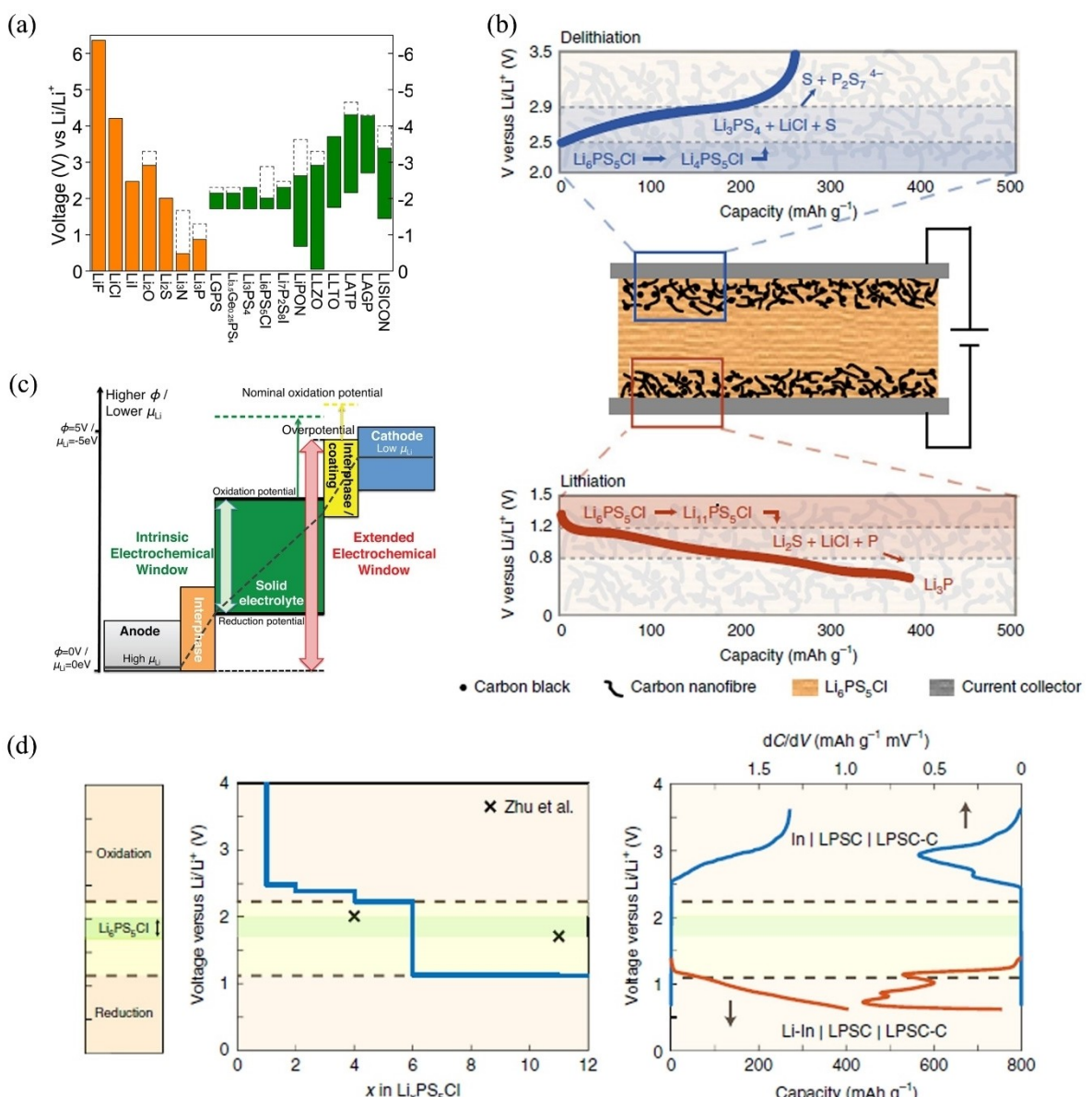
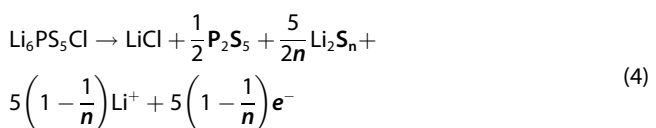


**Figure 7.** a) Electrochemical window for different electrolytes and other materials. b) Schematic diagram of the REDOX electrochemical activity of LPSC. c) Schematic diagram of the electrochemical window. d) Differential capacitance curve. a,c) Reproduced from Ref. [47c] with permission. Copyright (2015) American Chemical Society. b, d) Reproduced from Ref. [47a]. Copyright (2020) The Author(s), under exclusive licence to Springer Nature Limited.

structural design are expected to improve the compatibility with lithium argyrodite SSEs.

### 3.3. Stability with Cathode Materials

Recent studies showed that the specific capacity of ASSLBs had a rapid decay process after long-term cycling, which is closely related to side reactions between the cathode and lithium argyrodite SSEs, especially for oxides cathodes.<sup>[8a]</sup> Boulineau et al. assembled an ASSLB with Li<sub>6</sub>PS<sub>5</sub>Cl as the electrolyte, Li<sub>4</sub>Ti<sub>5</sub>O<sub>12</sub> as the negative electrode, 54 wt% LiCoO<sub>2</sub>/36 wt% Li<sub>6</sub>PS<sub>5</sub>Cl as the positive electrode.<sup>[50]</sup> It is found that there is an irreversible capacity decay with a value of ~20% in the first cycle, which can be ascribed to the appearance of the space charge layer and the diffusion of cobalt in the electrolyte. This is a typical electrochemical characteristic of the combination of sulfide electrolyte and uncoated LiCoO<sub>2</sub>. XPS characterizations showed that the Li<sub>6</sub>PS<sub>5</sub>Cl in the LiCoO<sub>2</sub> cathodes will be partially decomposed into LiCl, P<sub>2</sub>S<sub>5</sub>, and polysulfide, as depicted by Equation (4).<sup>[50]</sup> The appearance of LiCl is responsible for the increase of interface resistance.<sup>[49]</sup>



When Li<sub>6</sub>PS<sub>5</sub>Cl was mixed with other oxide cathodes such as NCM and LiMn<sub>2</sub>O<sub>4</sub>, Li<sub>6</sub>PS<sub>5</sub>Cl at the interface would be oxidized to elemental sulfur, P<sub>2</sub>S<sub>x</sub> ( $x < 5$ ), lithium polysulfide, LiCl, and phosphate.<sup>[51]</sup> The decomposition rate of lithium argyrodite SSEs can be slowed down by decreasing the contact area between SSEs and active cathodes. For example, a vapor-grown carbon fiber (VGCF) with a relatively small specific surface area of 24 m<sup>2</sup> g<sup>-1</sup> is used to replace carbon black (CB, 80 m<sup>2</sup> g<sup>-1</sup>).<sup>[52]</sup> The ASSLBs using VGCF showed much lower decomposition capacity and slower decomposition kinetics than that of the cell using CB. The sharp vertical voltage line at the end of the plateau of the SSE-CB composite also indicates a complete reaction of SSE in the composite, while the VGCF composite shows a higher polarization, indicating a decreased decomposition rate. Meanwhile, the functional groups on the surface of carbon additives play a negative role in the interface between SSEs with conducting agents. Park et al. found that the oxygen-containing surface functional groups on the carbon directly participate in the side reactions with the SSEs through forming insulating decomposition products, thus leading to poor electrochemical performance of ASSLBs.<sup>[53]</sup> While the graphitic hollow nanocarbon with fewer surface functional groups can alleviate the formation of an insulating layer at the interface of SSEs during the initial cycles.

The layered transition metal oxide cathode Li<sub>1+x</sub>(Ni<sub>1-y-z</sub>Co<sub>y</sub>Mn<sub>z</sub>)<sub>1-x</sub>O<sub>2</sub>(NCM) is an ideal high-capacity cathode material for ASSLBs. But the main drawback of NCM is that high states of charge easily lead to the release of O<sub>2</sub>. When combined with Li<sub>6</sub>PS<sub>5</sub>Cl electrolyte to assemble an ASSLB, NCM cathode still

releases CO<sub>2</sub> and O<sub>2</sub> originated from LiCO<sub>3</sub> pollutants and high-charge itself. It is worth noting that the gas production from Li-In/Li<sub>6</sub>PS<sub>5</sub>Cl/NCM cell is significantly lower than the liquid electrolytes-based LIBs or β-Li<sub>3</sub>PS<sub>4</sub> electrolytes-based ASSLBs. Therefore, Li<sub>6</sub>PS<sub>5</sub>Cl is more compatible with the NCM cathode compared with liquid electrolyte and β-Li<sub>3</sub>PS<sub>4</sub>.<sup>[54]</sup>

In comparison with oxide cathodes, sulfide-type cathodes are likely to be more compatible with argyrodites. Chen et al. assembled an ASSLB used with Li<sub>6</sub>PS<sub>5</sub>Br as the electrolyte, CuS as the cathode, and In-Li as the anode. This ASSLB exhibited a high discharge capacity of 650 mAh g<sup>-1</sup> at a current density of C/50.<sup>[55]</sup> X-ray diffraction analysis obtained at different discharge stages showed that the CuS electrode experienced a special reaction process in this ASSLB. Specifically, Li<sub>6</sub>PS<sub>5</sub>Br reversibly participated in the redox reaction during the charging and discharging of these ASSLBs. In the middle stage of discharge, Cu<sub>y</sub>Li<sub>6-y</sub>PS<sub>5</sub>Br was generated by the infiltration of Cu<sup>+</sup> into argyrodites. The concomitant volume change of CuS (ca. 80%) led to the separation of CuS from electrolytes and carbon additives. The decrease in ionic conductivity for newly-formed Cu<sub>y</sub>Li<sub>6-y</sub>PS<sub>5</sub>Br and the volume change of electrolytes would lead to poor cycling performance of ASSLBs. Yu et al. assembled ASSLBs with Li<sub>6</sub>PS<sub>5</sub>Cl as the electrolyte, Li<sub>2</sub>S with 20% LiI as the cathode, and In as an anode.<sup>[56]</sup> They found that Li<sub>6</sub>PS<sub>5</sub>Cl would react with the cathodic materials, which can be partially oxidized to LiCl, P<sub>2</sub>S<sub>5</sub>, thus delaying the mobility of Li<sup>+</sup>. While LiI was used as a protective layer to separate Li<sub>2</sub>S active substances and solid electrolyte particles, to some extent, improving the cycling performance of ASSLBs. Although sulfide-based cathode materials have a high performance in a specific capacity, the large volume change and unexpected side reactions during charging and discharging will result in the poor cycle performance of ASSLBs.

### 3.4. Stability with Liquid Electrolytes

Due to the hardness of SSEs, the interface contact between SSEs and electrodes is very hard to get the ideal output. In some cases, a certain amount of liquid electrolyte was added into the cathodic side to improve interface contact and cycle stability of ASSLBs, especially for metal oxides-based SSEs.<sup>[57]</sup> There are few studies on the stability of argyrodites in liquid electrolytes. The main reason is that lithium argyrodites containing halogen are unstable in commercial LP30 (1 M LiPF<sub>6</sub> in EC:DMC = 1:1) electrolytes.<sup>[58]</sup> Many amorphous mixtures appeared after soaking lithium argyrodite in LP30 at 40 °C for 3 weeks. However, the halogen-free lithium argyrodites that replace P with Si have higher stability for liquid electrolytes compared with conventional lithium argyrodite. For example, Holger et al. found that the crystal structure of Li<sub>2</sub>Si<sub>2</sub>P<sub>2</sub>S<sub>18</sub> did not change significantly, and no other visible side reactions occurred, even after soaking halogen-free lithium argyrodite into liquid electrolytes for more than three weeks.<sup>[58]</sup>

## 4. Synthetic Method

Until now, several synthetic methods for lithium argyrodite have been developed, mainly including the solid-state method and wet-chemical method. The most common synthetic method is the solid-state method, which includes two steps: ball milling and followed by the sintering process. Ball milling has been demonstrated to be the most effective technique to prepare fine powders of lithium argyrodite. The fine powders help realize intimate contact between SSEs and electrode materials during the assembling process of ASSLBs. Sintering can improve the crystallinity and ionic conductivity of lithium argyrodite SSEs. Compared with the solid-state method, the main drawback of the wet chemical method is that as-synthesized lithium argyrodite SSEs show relatively low ionic conductivity, which can be ascribed to the contamination from the organic solvent. However, the wet chemical method enables lithium argyrodite SSEs to closely contact with active materials to form a solid-solid interface, thus reducing the contact resistance of ASSLBs.

### 4.1. Solid-Phase Synthesis Method

The solid-state method is the most widely used method to synthesize lithium argyrodite. The conventional procedures of the solid-state method for lithium argyrodite SSEs include two steps: ball milling and annealing, which are illustrated in Figure 8(a). The solid-state synthesis method has the advan-

tages of solvent-free, high-yield, less-pollution, and low-cost. During the ball milling process, the raw materials undergo a series of changes, such as mixing, crushing, amorphization, and solid-state reaction.<sup>[8a]</sup> Ball milling can increase molecular contact and facilitate molecular diffusion. After the high-speed ball milling, the lithium argyrodite phase can be formed spontaneously without annealing.<sup>[45]</sup> If the energy is insufficient during the ball milling process, only the raw materials such as Li<sub>2</sub>S, P<sub>2</sub>S<sub>5</sub>, and LiX (X=Cl, Br, or I), are left after ball milling.<sup>[43a]</sup> The density of the balls is also a key parameter in synthesizing lithium argyrodite SSEs. The zirconia balls with the same size and high density can provide more energy than the agate balls with low density.<sup>[45]</sup>

Table 1 summarized the synthesized parameters including the milling parameters, annealing temperature, and conductivity for lithium argyrodite SSEs. As shown in Figure 8(b), extending the time of mechanical ball milling, to some extent, has a positive effect on the preparation of lithium argyrodite with high crystallinity. However, excessive extending of the grinding time has no help for the crystallinity and ionic conductivity of lithium argyrodite. Prasada et al. found that after grinding for 24 and 80 h, raw materials were still maintained as confirmed the XRD patterns, however, argyrodite crystal phases with similar crystallinity were obtained for both two samples after annealing at 550 °C.<sup>[59]</sup> Boulineau et al. tested the ionic conductivity of Li<sub>6</sub>PS<sub>5</sub>Cl with different ball grinding times.<sup>[45]</sup> They found that the ionic conductivity reached a maximum of  $1.33 \times 10^{-3}$  Scm<sup>-1</sup> through a 10 h ball grinding. This phenomenon is possibly related to those Li<sub>6</sub>PS<sub>5</sub>Cl particles

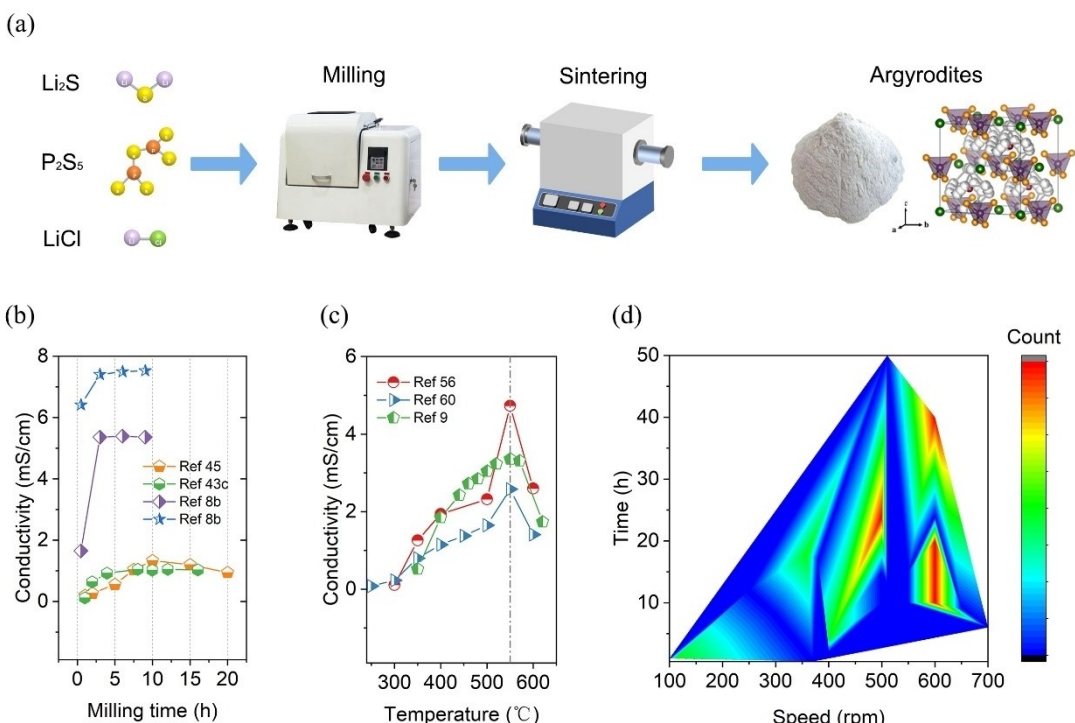


**Figure 8.** a) Schematic diagram of solid-state synthesis. Ionic conductivity of Li<sub>6</sub>PS<sub>5</sub>Cl with different parameters including b) ball-milling times and c) annealing temperature.<sup>[8b,9,43c,45,56,60]</sup> d) The frequency of ball milling parameters used in the literature. Red represents the highest frequency of use, and blue represents the lowest frequency of use.

**Table 1.** Synthesized parameters and ionic conductivities of lithium argyrodite SSEs via a solid-state method reported in the literature.

Compound	Milling speed [rpm]	Milling time [h]	Annealing temperature [°C]	Annealing time [h]	$\sigma_{Li^+}$ [S cm <sup>-1</sup> ] (Room temperature or 298 K except marked)	Ref.
$Li_6PS_5Cl$	600	20	—	—	$6.2 \times 10^{-4}$	[45]
	100	1	550	15	$3.38 \times 10^{-3}$	[9]
	110	1	550	10	$4.96 \times 10^{-3}$ (299.2 K) $(1.18 \pm 0.04) \times 10^{-3}$	[56]
	550	16	550	5		[22]
	650	12	550	2	$3.67 \times 10^{-3}$	[114]
	450	20	300	5	$2.0 \times 10^{-3}$	[54]
	550	15	550	5	$0.79 \times 10^{-3}$	[90]
	500	24	200	2	$1.30 \times 10^{-3}$	[100c]
	600	10	550	10	$1.6 \times 10^{-3}$	[44]
	500	24	300	3	$1.29 \times 10^{-3}$	[96]
$Li_6PS_5Br$	600	20	—	—	$4.6 \times 10^{-4}$	[45]
	550	15	550	5	$0.36 \times 10^{-3}$	[90]
	550	15	500	5	$1.03 \times 10^{-3}$	[83b]
	110	1	550	10	$2.58 \times 10^{-3}$	[60]
$Li_6PS_5I$	600	20	—	—	$1.9 \times 10^{-4}$	[45]

with a large specific surface area would be aggregated after an excessive extension of ball grinding time. Yu et al. also studied the effect of ball milling time on the formation of  $Li_6PS_5Cl$  argyrodites.<sup>[43c]</sup> The intensity of XRD diffraction peaks for  $Li_2S$  and  $LiCl$  decreases with the increment of grinding time. After 4 h of rotation at 550 rpm, the main peaks of the XRD match well with the  $Li_6PS_5Cl$  crystal structure. Additional XRD reflection disappears after 16 h milling, which indicates that pure  $Li_6PS_5Cl$  can be obtained by using mechanical grinding. The ionic conductivity of  $Li_6PS_5Cl$  argyrodites obtained by only ball milling for 16 h is only about  $1.0 \times 10^{-3}$  S cm<sup>-1</sup>, which can be further improved through an annealing process. Therefore, the appropriate ball grinding time should be optimized to improve the synthetic efficiency of lithium argyrodite powders. We have counted the frequency of use of ball milling parameters in some documents and shown it in Figure 8(d).

Noted that two main issues existing in high-energy ball milling to achieve lithium argyrodite powders. One is that high rotation speed (> 500 rpm) and a long grinding duration (> 10 h) are needed, which is time- and energy-consuming. The other is that it is difficult to obtain homogeneous materials due to the high-speed grinding process. Yu et al. developed a simple and optimized synthesis route to solve these problems.<sup>[56]</sup> In this method, the raw materials were ground initially at low rating speeding (such as 110 rpm) for 1 h, then anneals the mixed precursors at 550 °C for 10 h, resulting in argyrodite  $Li_6PS_5Cl$  with a high value of  $Li^+$  ionic conductivity up to  $4.96 \times 10^{-3}$  S cm<sup>-1</sup> at 26.2 °C. The high  $Li^+$  ionic conductivity of as-prepared  $Li_6PS_5Cl$  is mainly related to a uniform Cl atom distribution that maximizes the mobility of  $Li^+$  through this method, which is confirmed by EDX results. A similar result was also found by Zhang and co-workers.<sup>[38]</sup> They mixed ingredients manually in an agate mortar, then heated to 600 °C with a slow heat rate of 0.3 °C min<sup>-1</sup>. The ionic conductivity of as-prepared  $Li_6PS_5Cl$  with 2 wt% excess  $Li_2S$  is 1.8 mS cm<sup>-1</sup> at room temperature.

To further improve the high ionic conductivity of lithium argyrodite, the annealed process after mechanical ball milling is carried out to improve the crystallinity of lithium argyrodite.

More evidence demonstrated that the annealing parameters (such as time, temperature, and heating rate) play important roles in determining the ionic conductivity of lithium argyrodite, as shown in Figures 8. For example, when the sintering temperature is below 460 °C, it is difficult to obtain the pure phase of argyrodites.<sup>[9]</sup> With the further increase of sintering temperature, the intensity of XRD diffraction peaks of the impurities decreased gradually.<sup>[43b,45]</sup> Pure  $Li_6PS_5Cl$  crystals were obtained after the precursors were treated at 480 °C for 10 h and 550 °C for 10 h. A temperature higher than 620 °C is not suitable for obtaining high-purity  $Li_6PS_5Cl$  electrolytes, which can be attributed to that  $LiCl$ ,  $Li_2S$ , and unknown phases appear as the sintering temperature exceeding 620 °C.<sup>[45]</sup>

In addition, sintering time also plays an important role in determining the ionic conductivity of  $Li_6PS_5Cl$  electrolytes. If the annealing time is too short, raw materials cannot be fully transformed into argyrodites. With the increment of annealing time, the ionic conductivity of argyrodite slowly increases until reaching its maximum value. As the sintering time further increases, a decrease in ionic conductivity is found, which may be related to the evaporation of lithium.<sup>[60]</sup> Moreover, the heating rate is also a key parameter in the synthesis of lithium argyrodite. Increasing the heating rate helps to reduce the impurities. This phenomenon is explained by the fact that  $P_2S_5$  on the pellet surface becomes liquid during heating. If the heating rate is slow,  $P_2S_5$  will flow out of the sample. On the contrary,  $P_2S_5$  will infiltrate the sample to further react.<sup>[45]</sup>

It should be mentioned that the disorder of the anion sites (such as halogens and  $S^{2-}$ ) plays an important role in the ionic conductivity of lithium argyrodite. The disorder of the anion sites is strongly related to the time of crystallization and cooling rate. Gautam and co-workers systematically studied the effect of the synthesis process on the structure and ion migration of  $Li_6PS_5Br$  by using liquid nitrogen to control the cooling rate.<sup>[61]</sup> They found that  $Li_6PS_5Br$  with relatively high crystallinity can be achieved through rapid heat treatment within 1 min. The rapid cooling process leads to higher Br<sup>-</sup>/S<sup>2-</sup> dislocations. The ionic conductivity of the  $Li_6PS_5Br$  sample cooled rapidly is larger than that of the sample cooled slowly.

Besides the common solid-state synthesis method listed above, several new solid-state methods had been developed to synthesize lithium argyrodite with exceptionally high ionic conductivity. For example, Jung et al. synthesized halogen-rich lithium argyrodite  $\text{Li}_{5.5}\text{PS}_{4.5}\text{Cl}_{1.5}$  with the super high ionic conductivity of  $10.2 \text{ mScm}^{-1}$  (at  $25^\circ\text{C}$ ) using ultimate energy mechanical alloying and rapid thermal annealing.<sup>[8b]</sup> The high ionic conductivity can be attributed to high crystallinity over 82% of  $\text{Li}_{5.5}\text{PS}_{4.5}\text{Cl}_{1.5}$  via this new solid-state synthesis method. In this new approach, the ultimate-energy mechanical alloying process integrates mixing, glassification, and crystallization processes into a one-pot process, which can provide a 49 G-force milling energy, thus producing the lithium argyrodite powders with a crystallinity of ~70%. In addition, subsequent rapid thermal annealing using an infrared lamp further increases the crystallinity of lithium argyrodite up to 82% within 25 min.

Overall, the ionic conductivity of lithium argyrodite SSEs via the solid-state synthesis is relatively high as compared to other methods, e.g., wet chemical method, which is mainly ascribed to the less impurity content in argyrodites. During the solid-state synthesis method, the subsequent sintering process is necessary, and more evidence demonstrates that the sintering parameters play direct roles in the crystallinity of argyrodites. Although the solid-phase synthesis method for lithium argyrodite is easy to scale to industrial grade, there are still many obstacles hindering the wide application, such as low-quality, high-energy consumption, and time-consuming.

#### 4.2. Wet-Chemical Method

The wet chemical method shown in Figure 8(a) is considered as the effective and low-cost method to synthesize lithium argyrodite SSEs. In addition, the wet chemical method has the advantage of effectively morphological and structural control,

thus enabling us to fabricate thin-film SSEs. For example, solid electrolytes are easy to coat the surface of the active material particles during the liquid phase synthesis process to form a well-contacted interface, thus reducing the interface resistance. An apparent disadvantage prevails among the wet chemical methods, that is, the organic solvent is difficult to remove completely in the subsequent process, leading to an increase in grain boundary resistance and a decrease in ionic conductivity of SSEs. Therefore, choosing a suitable and easy-to-remove solvent is of great significance for improving ionic conductivity and reducing grain boundary. Common solvents used in the wet-chemical method are tetrahydrofuran (THF), ethyl acetate (EA), ethyl propionate (EP)-ethanol solution, and ethanol (EtOH) (Table 2).

EtOH with its property of low boiling point can reduce the side reaction between the electrolytes and active materials during drying, which is beneficial to improve the performance of ASSLBs. Yubuchi et al. synthesized a  $\text{Li}_6\text{PS}_5\text{Cl}$  SSE with a high lithium-ionic conductivity via a dissolution-reprecipitation method by using ethanol solution.<sup>[62]</sup> In this dissolution-reprecipitation approach, solid electrolytes ( $\text{Li}_6\text{PS}_5\text{Cl}$ ) are firstly synthesized by mechanical grinding using a planetary ball mill. And then, as-prepared  $\text{Li}_6\text{PS}_5\text{Cl}$  SSEs are dissolved in ethanol to produce precursor solutions. After evaporating the homogeneous ethanol solution, the  $\text{Li}_6\text{PS}_5\text{Cl}$  SSEs with an ionic conductivity of  $1.4 \times 10^{-5} \text{ Scm}^{-1}$  at room temperature can be achieved. The low conductivity of  $\text{Li}_6\text{PS}_5\text{Cl}$  SSEs may be related to the content of residual EtOH. Yubuchi et al. further added  $\text{LiCoO}_2$  particles into the  $\text{Li}_6\text{PS}_5\text{Cl}$  SSEs via ethanol solution, then SSEs uniformly coated on  $\text{LiCoO}_2$  to form a favorable electrode-electrolyte interface with a large contact area. An all-solid-state cell using the  $\text{Li}_6\text{PS}_5\text{Cl}$  SSEs-coated  $\text{LiCoO}_2$  operated as a rechargeable battery and showed the initial discharge capacity of  $45 \text{ mAhg}^{-1}$  at  $25^\circ\text{C}$ . Reducing the dissolution time in alcoholic solvents can reduce the content of residual organic solvent while increasing drying temperature can increase the

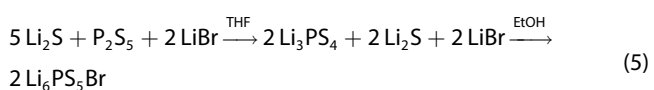
**Table 2.** Liquid phase synthesis parameters and ionic conductivity reported in the literature.

Compound	Rotating speed and time	Solution	Drying temperature [°C]	Annealing temperature [°C]	$\sigma_{\text{Li}^+} [\text{Scm}^{-1}]$	Ref.
$\text{Li}_6\text{PS}_5\text{Cl}$	600 rpm/45 h	EtOH	80	–	$1.4 \times 10^{-5}$ (298 K)	[62]
	600 rpm/10 h	EtOH	180	550 (10 h)	$1.0 \times 10^{-5}$ (303 K)	[109]
	–	EA	30	550 (5 h)	$1.1 \times 10^{-5}$ (298 K)	[65]
	600 rpm/45 h	EtOH	80	–	$1.4 \times 10^{-5}$ (298 K)	[63]
	–	THF, EtOH	140	550 (6 h)	$2.4 \times 10^{-5}$ (300 K)	[31]
	–	ACN or THF	90	200	$0.34 \times 10^{-5}$ (RT)	[115]
	600 rpm/40 h	EtOH + EA	150	–	$4 \times 10^{-5}$ (RT)	[116]
	–	EtOH	170	550 (6 h)	$1.9 \times 10^{-3}$ (RT)	[117]
	–	EP, EtOH	180	–	$3.4 \times 10^{-5}$	[66]
	600 rpm/45 h	EtOH	80	–	$5.5 \times 10^{-5}$ (298 K)	[63]
$\text{Li}_6\text{PS}_5\text{Br}$	–	THF, EtOH	150	550	$1.94 \times 10^{-5}$ (298 K)	[64a]
	–	THF, EtOH	150	550	$3.1 \times 10^{-5}$ (298 K)	[64b]
	–	THF, EtOH	140	550 (6 h)	$1.9 \times 10^{-5}$ (300 K)	[31]
	–	ACN or THF; EtOH	90	200	$0.31 \times 10^{-5}$ (RT)	[115]
	600 rpm/45 h	EtOH	80	–	$1.9 \times 10^{-5}$ (298 K)	[63]
$\text{Li}_6\text{PS}_5\text{I}$	–	THF, EtOH	140	550 (6 h)	$2 \times 10^{-6}$ (300 K)	[31]
	–	ACN or THF; EtOH	90	200	$0.29 \times 10^{-4}$ (RT)	[115]
	–	EtOH	90	200	$1.1 \times 10^{-4}$ (RT)	[118]
$\text{Li}_7\text{PS}_6$	–	EtOH	90	–	–	–

\* Ethyl acetate (EA), ethyl propionate (EP), acetonitrile (ACN), tetrahydrofuran (THF), ethyl alcohol (EtOH).

crystallinity and decrease activation energy of lithium argyrodite SSEs, which is beneficial to improve ionic conductivity.<sup>[63]</sup> Zhang et al. directly synthesized lithium argyrodite  $\text{Li}_6\text{PS}_5\text{Cl}$  in a one-step wet-chemical method that used ethanol as a solvent without ball-milling process, and the ionic conductivity of ball-milling-free  $\text{Li}_6\text{PS}_5\text{Cl}$  is  $2.1 \times 10^{-4} \text{ S cm}^{-1}$  at room temperature, which is inferior to  $\text{Li}_6\text{PS}_5\text{Cl}$  synthesized by the ball-milling method. However, the ability of Li dendrites suppression for this  $\text{Li}_6\text{PS}_5\text{Cl}$  SSEs is highly comparable to that of solid-state sintered  $\text{Li}_6\text{PS}_5\text{Cl}$  SSE.

Figure 9 shows the synthesis procedure of lithium argyrodite electrolyte with high conductivity via a simple solution process using THF and EtOH dual solvents.<sup>[64]</sup> The reaction in the liquid phase is shown in Equation (5).



In this wet-chemical process, EtOH cannot be used at first which is ascribed to that  $\text{P}_2\text{S}_5$  precursors is unstable in EtOH, being unfavorable for growing a single phase of  $\text{Li}_6\text{PS}_5\text{Br}$ . When THF was employed as the solvent,  $\text{P}_2\text{S}_5$  precursors cannot react with THF. In this case, intermediate products including  $\text{Li}_3\text{PS}_4$ ,  $\text{Li}_2\text{S}$ , and  $\text{LiBr}$  can be achieved. After the evaporation of THF solvent, EtOH was introduced into this reaction system, thus a single phase of  $\text{Li}_6\text{PS}_5\text{Br}$  was formed. In this method, THF decreases the reaction time by several hours compared with other solvents such as dimethoxymethane (DME, 10 days) or acetonitrile (ACN, 2 days). Noted that THF with its lower boiling point can be removed rapidly. The ionic conductivity of as-prepared  $\text{Li}_6\text{PS}_5\text{Br}$  can increase up to  $3.1 \times 10^{-3} \text{ S cm}^{-1}$  (at  $25^\circ\text{C}$ ) after further heat treatment at  $550^\circ\text{C}$ .

Ethyl acetate (EA) was also used as the solvent to prepare argyrodites  $\text{Li}_6\text{PS}_5\text{Cl}$  solid electrolyte via a liquid-phase process.<sup>[65]</sup> The ionic conductivity of  $\text{Li}_6\text{PS}_5\text{Cl}$  heated by  $550^\circ\text{C}$  reaches up to  $1.1 \times 10^{-3} \text{ S cm}^{-1}$  at room temperature, which is

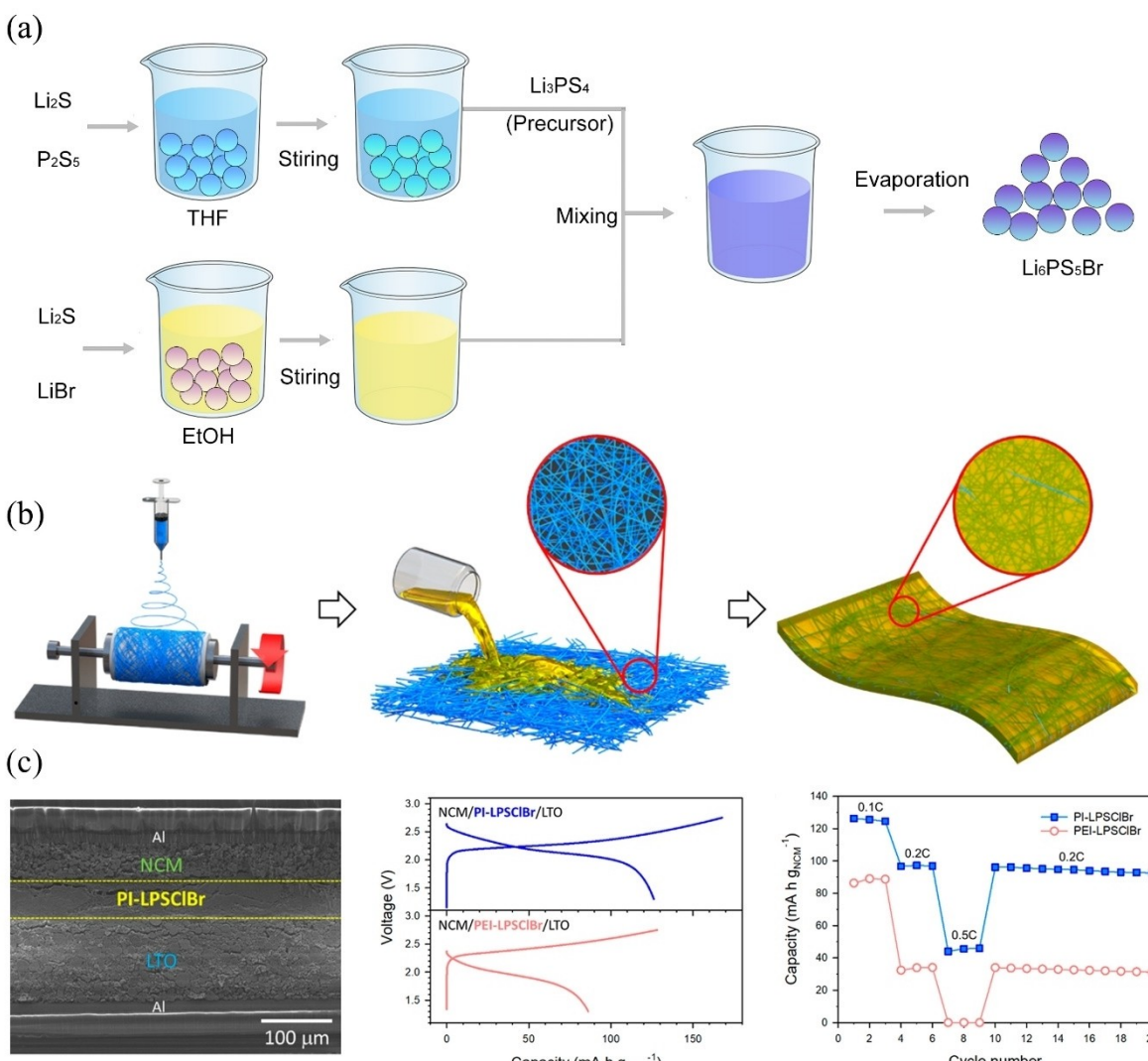


Figure 9. a) Schematic diagram of  $\text{Li}_6\text{PS}_5\text{Br}$  liquid phase synthesis.<sup>[64b]</sup> b) The preparation process of composite electrolyte containing PI membrane. c) SEM cross-section of all-solid-state cells and electrochemical properties. Reproduced from Ref. [103] with permission. Copyright (2020) American Chemical Society.

highly comparable to lithium argyrodite achieved by the mechanical milling process. This work demonstrated that the advantage of EA introduction of achieving high-performance argyrodites  $\text{Li}_6\text{PS}_5\text{Cl}$  without additional mechanical grinding. Recently, Shunjiro et al. proposed a novel ultrasonic solid solution process without mechanical grinding to synthesize  $\text{Li}_6\text{PS}_5\text{Br}$ .<sup>[66]</sup> In this synthetic method, the precursors were ultrasonically treated with ethyl propionate (EP). Ultrasound leads to the reaction between  $\text{Li}_2\text{S}$  and  $\text{P}_2\text{S}_5$  to form a  $\text{PS}_4^{3-}$  unit, thus an intermediate of  $\alpha\text{-Li}_3\text{PS}_4$  in a white suspension can be achieved. Absolute ethanol is then added to the white suspension to form a green and transparent precursor solution. The transparent solution is heated for 3 h at 423 or 453 K and removed the solvent under vacuum. The main phase of the synthesized product is  $\text{Li}_6\text{PS}_5\text{Br}$ , and the ionic conductivity is  $3.4 \times 10^{-5} \text{ Scm}^{-1}$  at room temperature. This method is time-saving with a total production time of only 4 h. However, the ionic conductivity of the product is relatively low. Hence, this ultrasound method may be more suitable for coating active materials or making composite electrodes.

Up to now, the wet-chemical method was widely used to synthesis lithium argyrodite SSEs with their merits of high efficiency and low cost. The ionic conductivities of lithium argyrodite SSEs via the wet-chemical method are still lower than that of lithium argyrodite SSEs via the solid-state synthesis method. The unwanted impurities would be produced during the wet-chemical process, which has been demonstrated to injury the ionic conductivity. Organic solvents with their different boiling points and solubility to intermediates from the wet-chemical process have been demonstrated to play an important role in ionic conductivity of as-produced lithium argyrodite SSEs and reducing the impurities. It should be noted that if the organic solvent is not completely removed during the synthesized process, resulting in an increase in grain boundary resistance and a decrease in ionic conductivity of SSEs. A suitable and easy-to-remove solvent is of great significance for improving ionic conductivity and reducing grain boundary. Overall, it is of great significance to develop the novel wet-chemical synthesis method with simple steps and fewer impurities for producing high-performance lithium argyrodite on a large scale.

## 5. Applications in ASSLBs

### 5.1. Interface Challenges and Strategies

#### 5.1.1. Anode Side

Metal lithium has a high theoretical specific capacity ( $3860 \text{ mAh g}^{-1}$ ) and a low potential ( $-3.04 \text{ V}$  vs. SHE), which is considered the most promising anode material for ASSLBs. Unfortunately, the uneven deposition of Li metal generates many dendrites, and Li dendrites will infiltrate along the crystal boundaries and pores of SSEs, resulting in an internal short circuit.<sup>[67]</sup> Li dendrites, therefore, are considered the most serious issues on ASSLBs.<sup>[67b,68]</sup> Up to now, a series of methods

have been developed to reduce the interface resistance between SSEs and metal Li anode in ASSLBs.<sup>[67a,68d,69]</sup>

Simon et al. evaluated the application of poly (ethylene oxide) (PEO) based SPEs as intermediate layers to protect the decomposition of argyrodites-type  $\text{Li}_6\text{PS}_5\text{Cl}$  at the interface between lithium metal anode and electrolyte.<sup>[70]</sup> It is observed that the solid polymer electrolyte interface (SPIE) was formed at the SPE| $\text{Li}_6\text{PS}_5\text{Cl}$  interface, which was mainly composed of lithium fluoride (LiF) and polysulfide ( $\text{--S}^0\text{--}$ ). LiF is a key component that can stabilize the SEI layer. Zhao et al. proposed a strategy for a fluorinated  $\text{Li}_6\text{PS}_5\text{Cl}$  argyrodite to enhance the interfacial stability toward the Li metal anode. The condensed and highly fluorinated interface was formed in situ with a self-healing property, hence a Li metal symmetric cell employing the fluorinated  $\text{Li}_6\text{PS}_5\text{Cl}$  SSE enables ultra-stable Li plating/stripping over 250 h at a superhigh current density of  $6.37 \text{ mA cm}^{-2}$  and a cutoff capacity of  $5 \text{ mAh cm}^{-2}$ .<sup>[71]</sup> Li et al. developed an efficient strategy to fabricate robust and stable SEI at the Li/SE interface by using LiCl-rich argyrodite SE ( $\text{Li}_6\text{PS}_5\text{Cl}\text{-LiCl}$ ) and a trace amount of propylene carbonate (worked as a wetting agent).<sup>[72]</sup> The formed SEI serves as a buffer layer to passivate the interfacial reactions and suppress Li dendrite growth and also acts as a bridge for Li-ion conduction to reduce the contact resistance. Therefore, the corresponding Li||Li symmetric cells can be cycled over 1000 h at a current density of  $0.2 \text{ mA cm}^{-2}$ . Recently, Chen and co-workers employed DFT calculations to study the interfacial properties of metal Li anode/ $\text{Li}_6\text{PS}_5\text{Cl}$  SSE interface system and buffer layers ( $\text{Li}_2\text{S}$ ) effects. They found that the  $\text{Li}_2\text{S}$  buffer layer prevented the decomposition of  $\text{PS}_4^{3-}$  tetrahedral by inhibiting the diffusion of S or Cl atoms, thus improving the stability of the Li/ $\text{Li}_6\text{PS}_5\text{Cl}$  interface.<sup>[73]</sup> Furthermore, the electronic structure of the interface shows that when the buffer layer is added, it is not easy to form interphase on  $\text{Li}_6\text{PS}_5\text{Cl}$  SSEs.

The inhomogeneous stripping/plating of lithium metal is the main reason for dendrite formation.<sup>[68e,74]</sup> Controlling the structure of electrodes or electrolytes to promote the nucleation and uniform growth of lithium is an effective method to inhibit the formation of dendrites. Lee et al. used Ag-C nano-composite electrodes without additional Li metal to achieve Li-regulated growth.<sup>[10]</sup> The C layer can separate Li from SE, as shown in Figure 10(a and b). Nano-Ag would alloy with Li to form a uniform and dense Li-Ag layer without dendrites. The assembled full battery achieves an ultra-high cycle life of 1,000 times as shown in Figure 10(c). Because the negative electrode does not contain extra lithium, the ASSLB has a very high energy density over  $900 \text{ Wh L}^{-1}$ . Li et al. dissolved  $\text{Li}_6\text{PS}_5\text{Cl}$  in ethanol solution and then poured it into the pore of wood to form a composted SSE.<sup>[75]</sup> By confining the  $\text{Li}^+$  to the channel perpendicular to the electrodes, the transmission path of  $\text{Li}^+$  is regulated in this newly-formed SSE, which enables the uniform stripping and plating of lithium at the interface (Figure 11a-d).

Among the alloy-type anode materials, silicon exhibits a high theoretical specific capacity ( $4200 \text{ mAh g}^{-1}$  for  $\text{Li}_{4.4}\text{Si}$ ) and a low operating voltage of  $0.3 \text{ V}$  (vs. Li/Li $^+$ ). At this point, silicon may be a promising alternative anode material to graphite for the next generation of LIBs.<sup>[76]</sup> Despite its extremely high

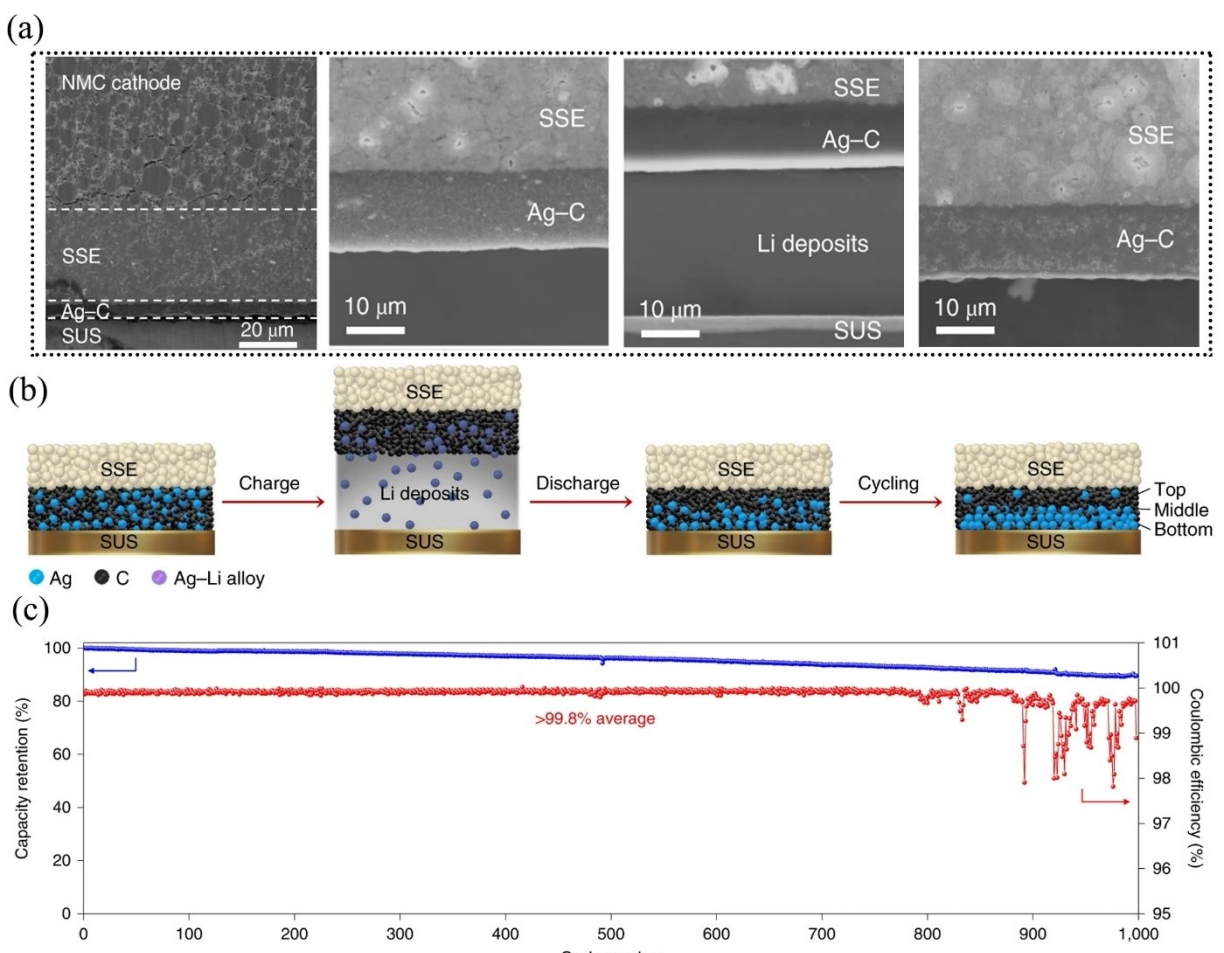


**Figure 10.** a) Cross-sectional SEM images of the all-solid-state battery containing Ag-C composite anode. b) Schematic diagram of Li plating and stripping process on current collector containing Ag-C composite anode. c) Cycle performance of Ag-C|SSE|NMC battery. Reproduced from Ref. [10] with permission. Copyright (2020) The Author(s), under exclusive licence to Springer Nature Limited.

capacity, the massive volume change (~400%) during lithification and de-lithium hinders the practical application of silicon in LIBs, resulting in the pulverization of silicon particles and the loss of electrode contact.<sup>[77]</sup> Kim et al. also found that liquefied  $\text{Li}_6\text{PS}_5\text{Cl}$  osmotic electrodes show a high charging capacity of  $3246 \text{ mAh g}^{-1}$  due to the close contact between silicon and  $\text{Li}_6\text{PS}_5\text{Cl}$ .<sup>[77b]</sup> Cangaz et al. fabricated a columnar silicon anode by a physical vapor deposition process on an argyrodite-type electrolyte ( $\text{Li}_6\text{PS}_5\text{Cl}$ ,  $3 \text{ mScm}^{-1}$ ).<sup>[78]</sup> The as-fabricated ASSLBs were cycled more than 100 cycles with a high coulombic efficiency of 99.7–99.9% with a high areal loading of  $3.5 \text{ mAh cm}^{-2}$ . Overall, alloy-type anodes hold promise for enabling high-energy ASSLBs, but their substantial volume changes during charge/discharge lead to structural and mechanical degradation of ASSLBs, presenting the main issue which should be solved preferentially.

### 5.1.2. Cathode Side

To improve the electrochemical performance of ASSLBs, the interface with a large contact area between the electrodes and

SSEs is preferential. The formation of an interface with a large contact area can optimize the ion conductive path. For conventional electrodes, active materials and SSEs are well-mixed in one electrode, however, many cracks and holes have existed. For the electrodes with SSEs-coated active materials, the active material particles are in close contact with SSEs. As a result, an ideal ionic conductive path is formed among the active material particles. Besides, active material particles contact each other directly, thus forming effective electron conductive paths.<sup>[63,79]</sup> The contact area between active materials and SSEs increases about 2.6 times after the SSEs coating.<sup>[80]</sup> Zhang et al. developed a solvent-mixing process to form the PTO-interphase- $\text{Li}_6\text{PS}_5\text{Cl}$  “core-shell” structure. This process promotes the formation of a microstructure for efficient charge transport which enables an electrode-level ASSLB with a specific energy of  $302 \text{ Wh kg}^{-1}$ .<sup>[6a]</sup>

It should be noted that adding excess SSEs into the cathode can increase the electrochemical performance of active materials, however, it would inevitably lead to a decrease in the volumetric energy density of ASSLBs. How to use a small quantity of SSEs in cathode on a simple premise of ensuring a good coating effect is the key to solving the current issues of

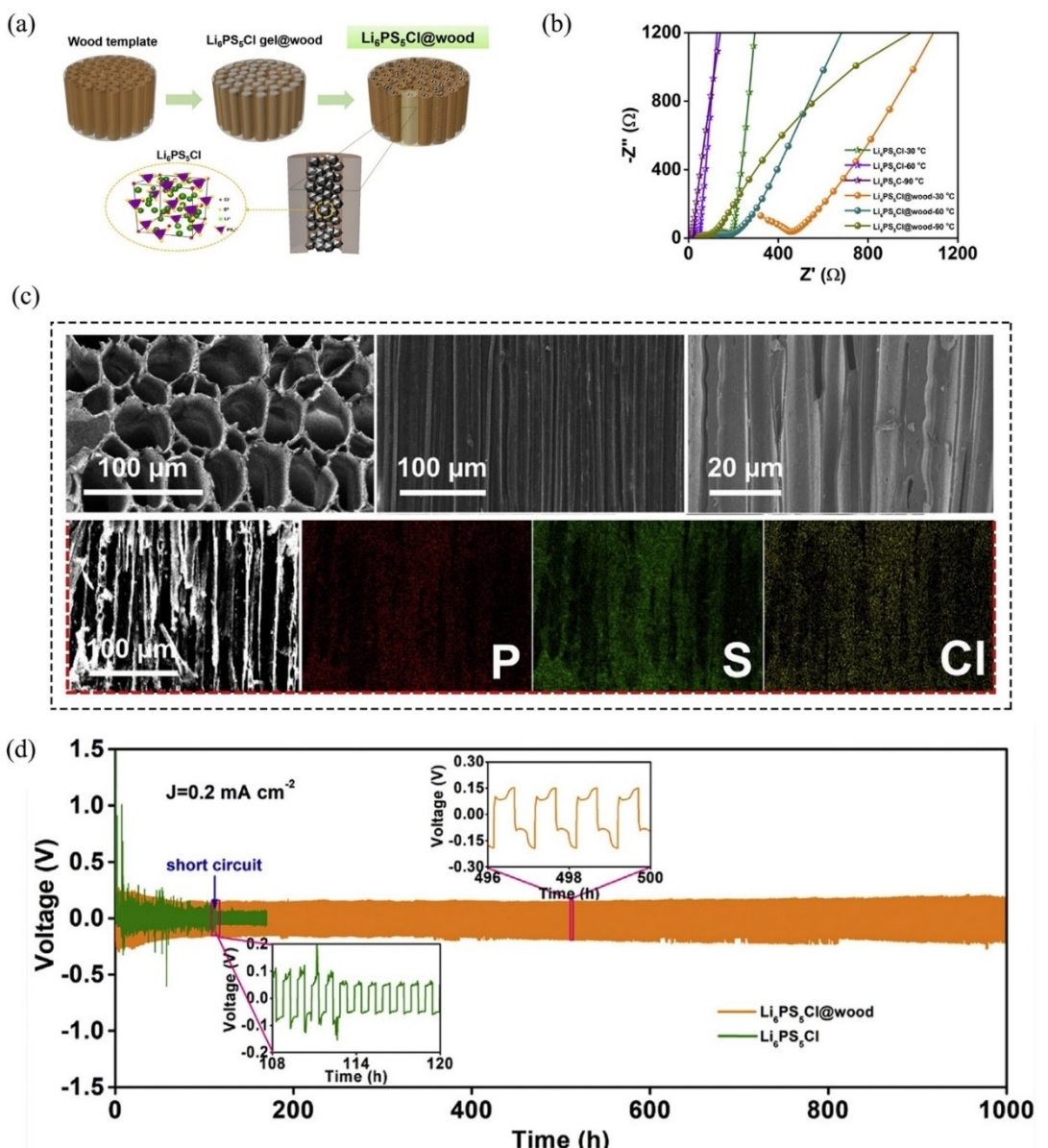


**Figure 11.** a) Schematic diagram of Li<sub>6</sub>PS<sub>5</sub>Cl @wood SE prepared by template method. b) EIS spectra of Li<sub>6</sub>PS<sub>5</sub>Cl and Li<sub>6</sub>PS<sub>5</sub>Cl@wood SEs at various temperatures of 30, 60, and 90 °C. c) SEM images of Li<sub>6</sub>PS<sub>5</sub>Cl@wood SE infused with SE in wood channels and EDS mappings of P, S, and Cl. d) Voltage profiles of symmetric cells for Li<sub>6</sub>PS<sub>5</sub>Cl (green) and Li<sub>6</sub>PS<sub>5</sub>Cl@wood (orange) SEs at a current density of 0.2 mA cm<sup>-2</sup> with a fixed areal capacity of 0.1 mAh cm<sup>-2</sup>. Reproduced from Ref. [75] with permission. Copyright (2020) Published by Elsevier B.V.

the low volumetric energy density of ASSLBs. Adding an appropriate number of dispersants in the liquid phase synthesis process may be a good choice. This is because of that the addition of dispersants can reduce the particle size of as-synthesized SSEs to make them more uniformly coated on the active material particles.<sup>[124]</sup> Yubuchi et al. fabricated the rechargeable ASSLBs which used Li<sub>6</sub>PS<sub>5</sub>Cl or Li<sub>6</sub>PS<sub>5</sub>Br coated LiCoO<sub>2</sub> as a cathode through EtOH as the solvent.<sup>[62,63]</sup> The discharge capacity of as-fabricated ASSLBs reaches 45 mAh g<sup>-1</sup>, which is higher than that of Li<sub>3</sub>PS<sub>4</sub>-coated LiCoO<sub>2</sub>. Therefore, cathode coated with SSEs with high ionic conductivity can effectively improve the electrochemical performance of ASSLBs. Hwang et al. successfully coated Li<sub>6</sub>PS<sub>5</sub>Cl on the surface of

Li<sub>4</sub>Ti<sub>5</sub>O<sub>12</sub> material by using 200# Paint as the solvent, which significantly increased the interfacial contact area.<sup>[44]</sup> Li<sub>4</sub>Ti<sub>5</sub>O<sub>12</sub>/Li<sub>6</sub>PS<sub>5</sub>Cl/ Li ASSLBs have a high capacity of 158.4 mAh g<sup>-1</sup> after 250 cycles with excellent capacity retention of about 94.3%. 200# Paint with its low boiling point can be easily removed during the preparation process of the electrode to prevent side effects. More importantly, 200# Paint is inexpensive and non-toxic.

When the oxide cathodes directly contact with sulfide SSEs, the high electrochemical potential of the oxide cathodes will make Li<sup>+</sup> migrate from the SSEs to the oxide cathodes, thus forming a lithium-ion depletion layer in SSEs, i.e., space charge layer.<sup>[81]</sup> The appearance of the space charge layer leads to the

increment of interface resistance and sluggish lithium-ion transport across the solid electrode/electrolyte interface.<sup>[82]</sup> The interfacial issues can be alleviated by coating a buffer layer on the cathode, such as Li<sub>2</sub>O-ZrO<sub>2</sub>, Li<sub>3</sub>BO<sub>3</sub>, LiNbO<sub>3</sub>.<sup>[10,30b,83]</sup> These buffer layers can reduce the polarization and the interface resistance between the active positive materials and SSEs, thereby improving the electrochemical performance of cathode materials.<sup>[30b,83b]</sup> Among these coating layer materials, LiNbO<sub>3</sub> was demonstrated to be the most suitable candidate as the coating layers. This is because that LiNbO<sub>3</sub> has an acceptable ionic conductivity exceeding 10<sup>-6</sup> S cm<sup>-1</sup> at room temperature and can be easily synthesized by the wet method using ethanol as a solvent.<sup>[84]</sup> However, the scarcity of Nb makes the LiNbO<sub>3</sub> being expensive and unsuitable for mass production. Compared with LiNbO<sub>3</sub>, low-cost Li<sub>3</sub>BO<sub>3</sub> and Li<sub>2</sub>O-ZrO<sub>2</sub> are also good choices.<sup>[10,30b,83]</sup>

More evidence also showed that sulfides-based cathodic materials had good electrochemical compatibility with lithium argyrodite SSEs. MoS<sub>2</sub>, as a typical transition metal dihalides, has a high theoretical specific capacity (670 mAh g<sup>-1</sup>) and low cost, making it a more promising electrode material for LIBs.<sup>[85]</sup> Chen et al. reported that all-solid MoS<sub>2</sub>/Li<sub>6</sub>PS<sub>5</sub>Br/In-Li batteries have a high rate capability of up to 1 C and excellent capacity retention of 85% after 700 cycles, even though the irregular MoS<sub>2</sub> microstructures used in this literature.<sup>[86]</sup> Zhang et al. reported a composited electrode synthesized by coating Li<sub>6</sub>PS<sub>5</sub>Cl on MoS<sub>2</sub> nanosheets in an anhydrous ethanol solution.<sup>[88]</sup> Because the coating process takes place in a liquid solution, a larger area of contact between SSEs and MoS<sub>2</sub> can be realized. The corresponding all-solid MoS<sub>2</sub>/Li<sub>6</sub>PS<sub>5</sub>Cl/In-Li battery shows a high capacity and excellent cycling performance. For example, a capacity value of 350 mAh g<sup>-1</sup> for these ASSLBs can be achieved at a current density of 0.13 mA cm<sup>-2</sup>. As the current density increases to 1.04 mA cm<sup>-2</sup>, this ASSLB still preserves a specific capacity value of 241 mAh g<sup>-1</sup>.

Sulfur has attracted significant attention in all-solid-state Li-S batteries due to its high theoretical capacity and excellent compatibility with SSEs. However, the cycle life of liquid electrolyte-based Li-S batteries is limited due to the large volume change of sulfur during the cycles.<sup>[87]</sup> To solve the above issues, Wang et al. proposed an all-solid-state Li-S battery by employing Li<sub>6</sub>PS<sub>5</sub>Cl as both the active material and electrolyte with a Li-In alloy anode.<sup>[88]</sup> The positive composite electrode is obtained by ball milling Li<sub>6</sub>PS<sub>5</sub>Cl and multi-wall carbon nanotube (MWCNT) together, and the negative electrode is Li-In alloy. After 650 cycles at 56 mA g<sup>-1</sup> at room temperature, the discharge capacity of this Li-S battery is as high as ~535 mAh g<sup>-1</sup>. The high reversible capacity of as-fabricated Li-S battery can be attributed to the followed reasons: Li<sub>6</sub>PS<sub>5</sub>Cl is oxidized to S, P<sub>2</sub>S<sub>5</sub>, and LiCl during the charging process, while S and part of P<sub>2</sub>S<sub>5</sub> are reduced to Li<sub>2</sub>S and Li<sub>3</sub>P during the discharging process, which is highly reversible at the low voltage.

Besides S, Li<sub>2</sub>S can also be used as cathode materials in all-solid-state batteries. This is because that the theoretical capacity of Li<sub>2</sub>S still reaches up to 1166 mAh g<sup>-1</sup>, which is nearly an order of magnitude higher than that of traditional metal

oxide/phosphate.<sup>[89]</sup> Wang et al. prepared ASSLBs by using Li<sub>6</sub>PS<sub>5</sub>Cl<sub>0.5</sub>Br<sub>0.5</sub> as electrolyte and Li<sub>2</sub>S as the cathode.<sup>[90]</sup> It was found that interface resistance was a key factor in limiting the electrochemical performance of ASSLBs.<sup>[91]</sup> However, the ionic conductivity at the interface of Li<sub>6</sub>PS<sub>5</sub>Cl<sub>0.5</sub>Br<sub>0.5</sub>-Li<sub>2</sub>S is much higher than that of Li<sub>6</sub>PS<sub>5</sub>Cl-Li<sub>2</sub>S and Li<sub>6</sub>PS<sub>5</sub>Br-Li<sub>2</sub>S.<sup>[92]</sup> Han and co-workers proposed a new bottom-up method to synthesize a Li<sub>6</sub>PS<sub>5</sub>Cl coated Li<sub>2</sub>S nanocomposite by using polyvinylpyrrolidone as the carbon precursor, Li<sub>2</sub>S as the active material, and Li<sub>6</sub>PS<sub>5</sub>Cl as the SSE dissolving in anhydrous ethanol, followed by a coprecipitation and high-temperature carbonization process.<sup>[93]</sup> The Li<sub>2</sub>S coated with Li<sub>6</sub>PS<sub>5</sub>Cl SSEs (with a particle size of ~4 nm) were uniformly distributed into a nanoscale carbon matrix. The homogeneous nanocomposite electrode has a large reversible capacity of 830 mAh g<sup>-1</sup> (71% utilization of Li<sub>2</sub>S) at 50 mA g<sup>-1</sup> after 60 cycles at room temperature even with a high mass loading of Li<sub>2</sub>S (~3.6 mg cm<sup>-2</sup>). This is a promising strategy to design a high mechanical strength, hybrid conductive nanocomposite electrode for good performance ASSLBs with Li<sub>2</sub>S cathode.

Recent studies also exhibited that conductive additives and binders were the important factors for cathode materials for lithium argyrodite-based ASSLBs. For example, the introduction of electronic conductive additives can accelerate the formation of oxidation products.<sup>[83c]</sup> Increasing the carbon content in the composite electrode composed of lithium argyrodite and active materials may decrease the energy density of ASSLBs, however, the increased carbon content in cathode may be beneficial to improve the rate capability of ASSLBs. In addition, binders also help to reduce strain/stress during the charging/discharging process of ASSLBs, which can promote electrical contact between active materials and collectors. The addition of a small amount of binder helps to improve the density and conductivity of the composite electrodes. However, the ionic conductivity of solid electrolytes can be reduced by adding a large amount of binder due to the poor ionic conductivity of the binder.<sup>[94]</sup> Nataly et al. found that adding a small amount of binder (0.5 wt% ethylcellulose) resulted in a higher capacity retention rate with a value of 91.7% after 10 cycles.<sup>[95]</sup> Zhang et al. systematically studied the effect of the content of ethylcellulose adhesives on the electrochemical performance of ASSLBs.<sup>[96]</sup> The composite cathode was prepared by mixed of LiNi<sub>0.8</sub>Co<sub>0.1</sub>Mn<sub>0.1</sub>O<sub>2</sub>, solid electrolyte (Li<sub>6</sub>PS<sub>5</sub>Cl), adhesive (ethylcellulose), and conductive additive (carbon black) in anhydrous ethanol through a traditional slurry coating method. The surface of NCM active material becomes coarser with the increased content of the binder. An appropriate content of binder can fill the gap between active particles, which may compensate for the volume change during charging and discharging. ASSLBs containing 1 wt% ethyl cellulose in the composite cathode show the highest electrochemical performance in energy and power density. The excessive content of the binder leads to the poor performance of ASSLBs, which is associated that the poor conductivity of binder hinders the migration of electrons and ions and reduces the utilization of active materials. It is still a challenge to find suitable adhesive polymeric binders that can be dispersed in common solvents

with sulfide electrolytes. Lee and co-workers report a thiolene click reaction used to graft styrene-butadiene-block copolymer with a carboxylic acid to obtain a new-type binder.<sup>[97]</sup> The click binder results in a uniform electrode slurry without destroying the structure of sulfide electrolytes, allowing ASSLBs to deliver good electrochemical performance. This work suggested that tuning polarity of functional binders elaborately established an important step forward in fabricating advanced ASSLBs on large scale.

Currently, significant breakthroughs have been made in lithium argyrodite-based ASSLBs, which have cast light on commercial applications. However, these extraordinary results on the electrochemical performance of ASSLBs are mainly based on the laboratory model cells. Also, reports on ASSLBs with attractive overall performance to meet the requirement from commercial use are still limited. For large-scale industrial applications, significant research and development efforts on assembling techniques for pouch-cell ASSLBs should be invested. Additionally, the in-depth unraveling of the interfaces including the anode materials/lithium argyrodite and cathodes/lithium argyrodite may provide valuable guidance for developing new-type lithium argyrodite with good compatibility for improving the overall electrochemical performance of ASSLBs.

## 5.2. Composite Electrolyte

The solid polymer electrolyte (SPE) generally refers to the combination of conductive lithium salt and the polymer matrix which has high solubility of the lithium salt. Generally, the polymer matrix of SPEs includes polyvinylidene fluoride-co-hexafluoropropylene (PVDF-HFP), polymethyl methacrylate (PMMA), and polyacrylonitrile (PAN).<sup>[98]</sup> Lithium salts include lithium perfluoroethylsulfonate ( $\text{LiC}_2\text{F}_5\text{SO}_3$ ), lithium perfluorobutylsulfonate ( $\text{LiC}_4\text{F}_9\text{SO}_3$ ), lithium triflate ( $\text{LiCF}_3\text{SO}_3$ , LiTf), lithium imide salts (LiTFSI), lithium bis(perfluoroethylsulfonyl)imide ( $\text{LiN}(\text{C}_2\text{F}_5\text{SO}_2)_2$  and (LiBETI)).<sup>[69,99]</sup> SPEs have excellent flexibility, convenient processing, lightweight, and low production cost. Common SPE based on PAN has a low ionic conductivity ( $10^{-5}$ – $10^{-7}\text{ S cm}^{-1}$ ) at room temperature, which severely limits its application in LIBs.<sup>[98b]</sup> The composite electrolyte (CPE) formed by adding inorganic solid electrolytes (ISE) combines the advantages of organic electrolytes and inorganic electrolytes, which has attracted significant attention.<sup>[98c,100]</sup>

ASSLBs assembled with CPE show good interface compatibility with Li metal anode, thus exhibiting excellent cycling performance. Zhang et al. dispersed  $\text{Li}_6\text{PS}_5\text{Cl}$  particles into PEO/anhydrous acetonitrile solution to achieve  $\text{Li}_6\text{PS}_5\text{Cl}$ -PEO CSEs after drying.<sup>[100c]</sup> Due to the excellent flexibility of PEO, the mechanical properties of  $\text{Li}_6\text{PS}_5\text{Cl}$  and the interface stability of electrodes/electrolytes are improved. When the PEO content in CSEs was 5 wt%, the capacity retention of the NCM/CSES/Li battery was increased to 91% after 200 cycles at 0.05 C. Simon et al. reported that PEO20: LiTFSI- $\text{Li}_6\text{PS}_5\text{Cl}$  CPEs with different content of  $\text{Li}_6\text{PS}_5\text{Cl}$  electrolyte filler is prepared by a slurry-based process. The CPEs have a high ionic conductivity of  $3.6\text{ mS cm}^{-1}$  compared to CPEs without  $\text{Li}_6\text{PS}_5\text{Cl}$  with a value of

$0.84\text{ mS cm}^{-1}$ .<sup>[100d]</sup> In-situ XPS results showed that the lithium metal reacted strongly with CPE to form LiF, polysulfides, and  $\text{Li}_3\text{PO}_4$  at the initial stage and was slow down over time, then an SEI consisting mainly of LiF and  $\text{Li}_2\text{S}$  was formed. The decomposition products influence the formation of the SEI at the lithium metal/CPE interface, leading to a reduced SEI resistance of  $3.3\text{ }\Omega\text{ cm}^2$  for the CPE40 sample compared to  $5.8\text{ }\Omega\text{ cm}^2$  for PEO20:LiTFSI sample at  $80^\circ\text{C}$ . The SPE/ISE interface makes the ion transport in the electrolyte more complicated. Furthermore, there is still no suitable theory of ion transport in composite electrolytes which should be explored in future.

A thin layer like SSEs is necessary for ASSLBs to improve high gravimetric and volumetric energy density. For large-scale applications, and SSE layer with a thickness of fewer than  $100\text{ }\mu\text{m}$  is required.<sup>[101]</sup> It is possible to coat the active materials with a thin SSE layer by the wet-slurry method. However, it is still difficult to obtain a uniform SSE coating with high mechanical strength on large scale.<sup>[102]</sup> CPEs composed of soft polymer separator materials and inorganic solid electrolytes are the promising choice for achieving a thin SSE with high mechanical strength and high ionic conductivity. For example, electrospinning polyimide (PI) nonwovens are suitable organic support materials with excellent mechanical strength, high porosity, small pore size, high thermal stability, and inherent flame retardance. Kim et al. reported that thin ( $40$ – $70\text{ }\mu\text{m}$ ) sulfide SSEs membranes with high conductivity ( $29\text{ mS cm}^{-1}$ , at  $30^\circ\text{C}$ ) were prepared by permeating solution-processable argyrodites ( $\text{Li}_6\text{PS}_5[\text{Cl}, \text{Br}]$ ) into highly porous PI NWs.<sup>[103]</sup> The high thermal stability of PI ( $\leq 500^\circ\text{C}$ ) enables it to be heated at temperatures below  $400^\circ\text{C}$ , which is necessary for solution-processed  $\text{Li}_6\text{PS}_5\text{Cl}_{0.5}\text{Br}_{0.5}$  to achieve a high conductivity of  $2\text{ mS cm}^{-1}$  at  $30^\circ\text{C}$ . Using  $\text{LiNi}_{0.6}\text{Co}_{0.2}\text{Mn}_{0.2}\text{O}_2$  (NCM)/graphite as active material and  $\text{Li}_6\text{PS}_5\text{Cl}_{0.5}\text{Br}_{0.5}$ -infiltrated PI membranes with  $40\text{ }\mu\text{m}$  thickness as an electrolyte, the full battery exhibits a high energy density of  $110\text{ Wh kg}_{\text{cell}}^{-1}$  and a negligible capacity degradation at  $180^\circ\text{C}$ , which indicates the excellent thermal stability of  $\text{Li}_6\text{PS}_5\text{Cl}_{0.5}\text{Br}_{0.5}$ -infiltrated PI membranes.

Lee et al. dissolved  $\text{Li}_6\text{PS}_5\text{Cl}$  into xylene and isobutyl isobutyrate to form a mixture, and then coated on a polyethylene terephthalate (PET) film by a doctor blading ( $t = 30\text{ }\mu\text{m}$ ).<sup>[10]</sup> The tap density of SSEs film was increased via a warm isostatic pressing machine (WIP). In addition, the obtained SSEs film has high mechanical strength and flexibility. The ASSLBs prepared using this film have an extremely high energy density ( $> 900\text{ Wh L}^{-1}$ ), and good cycling performance (over 1,000 times). Wang et al. also introduced the PVDF polymer into the  $\text{Li}_6\text{PS}_5\text{Cl}$  electrolyte and created a thin self-supporting electrolyte.<sup>[104]</sup> As an adhesive, PVDF fills in the voids formed in  $\text{Li}_6\text{PS}_5\text{Cl}$  particles, thus suppressing the growth of lithium dendrites effectively and improving the cycling stability of ASSLBs. However, owing to the low ionic conductivity of PVDF, PVDF may accumulate between  $\text{Li}_6\text{PS}_5\text{Cl}$  particles as excessive PVDF is added, which leads to the decrease of ionic conductivity of the composite electrolyte. Zhang et al. prepared a  $30\text{ }\mu\text{m}$  sulfide SE membrane by mechanized manufacturing technologies using highly conductive  $\text{Li}_{5.4}\text{PS}_{4.4}\text{Cl}_{1.6}$  SE powder

and PTFE powder (0.2 wt%). The obtained composite membrane is a 3D continuous PTFE network wrapped with SE particles with ultrahigh conductivity ( $8.4 \text{ mScm}^{-1}$  at  $25^\circ\text{C}$ ). Although PTFE is a nonconductive polymer, it occupies a minimal volume in the composite, maximizing the electrolyte phase content, which guarantees the  $\text{Li}^+$  conductive component in the membrane.<sup>[105]</sup> Liu et al. proposed a new strategy to obtain ultra-thin free-standing sulfide SSEs film, through coating a 5 nm thick homogeneous polydopamine layer on the  $\text{Li}_6\text{PS}_5\text{Cl}$  electrolyte particles in organic alkali solution.<sup>[106]</sup> The free-standing polydopamine-coated  $\text{Li}_6\text{PS}_5\text{Cl}$  thin film with a thickness of 35  $\mu\text{m}$  could be obtained by cold pressing. ASSLBs with the polydopamine-coated  $\text{Li}_6\text{PS}_5\text{Cl}$  thin film exhibit a discharge capacity of  $485.1 \text{ mAh g}^{-1}$  after 100 cycles at  $0.1 \text{ C}$  and  $25^\circ\text{C}$ , corresponding to a capacity retention of 78.5%.

In general, the total conductivity of the thin electrolyte films is lower than that found for bulk form lithium argyrodite. The extremely low conductivity of additives may be the main reason for this problem. Selecting the appropriate polymers and optimizing the synthesis process are expected to further improve the electrochemical performance of ASSLBs.

### 5.3. Other Factors Affecting the Performance of ASSLBs

At present, the ionic conductivity of argyrodite solid electrolyte can reach  $10^{-3} \text{ Scm}^{-1}$ , which is close to the ionic conductivity of the liquid electrolyte. Therefore, the ionic conductivity of lithium argyrodite SSEs is not the main factor for fabricating high-performance ASSLBs. During the fabrication process of ASSLBs, electronic additive agents, the size of argyrodites, and interface resistance were considered as the main factors limiting the performance of ASSLBs.

To maximize the capacity of the cathodic material in ASSLBs, it is usually necessary to add a certain amount of carbon and SSEs to the cathode to be convenient for electrons and lithium ions transport, respectively.<sup>[50]</sup> Stadler et al. found that carbon-coated  $\text{Li}_4\text{Ti}_5\text{O}_{12}$  (C-LTO) cathode added with 30 wt%  $\text{Li}_6\text{PS}_5\text{Br}$  can achieve the optimal ion and electron transport.<sup>[107]</sup> When the SSEs content is excessive, the gravimetric and volumetric capacities of ASSLBs can be largely decreased.<sup>[95]</sup> In this  $\text{LiCoO}_2/\text{Li}_6\text{PS}_5\text{Cl}/\text{In}$  battery, when the positive electrode contains 54 wt% LCO, the specific capacity of ASSLBs reaches the maximum value. If the proportion of LCO continues to increase, the specific capacity of the ASSLBs will gradually decline due to the poor ion permeability.<sup>[50]</sup>

Reducing the particle size of solid electrolytes can significantly enhance the electrochemical performance of ASSLBs. This is because that small-sized SSEs can increase the stacking density and contact area between solid electrolytes and active materials. At present, ball milling is a mature technique for lithium argyrodite SSEs with high ionic conductivity. As compared with manual grinding, ball milling can decrease the particle size of SSEs effectively and increase the contact area with active materials increases, which improves the initial capacity and cycling performance of ASSLBs.<sup>[43b,55b]</sup> Chen et al. prepared ASSLBs using sulfur as active cathode material and

$\text{Li}_6\text{PS}_5\text{Br}$  as a solid electrolyte.<sup>[108]</sup> The cathode composed of sulfur,  $\text{Li}_6\text{PS}_5\text{Br}$ , and super P carbon was prepared by two-step ball-milling at 500 rpm. The homogeneous cathode mixture with a particle size less than 100 nm was obtained. The S content in as-assembled all-solid  $\text{S}/\text{Li}_6\text{PS}_5\text{Br}/\text{In}-\text{Li}$  battery varies between 20 wt% and 40 wt%, with a maximum capacity of  $1460 \text{ mAh g}^{-1}$  (relative to the weight of sulfur), 50 cycles at  $\text{C}/10$  rate, and a reversible capacity of  $1080 \text{ mAh g}^{-1}$ .

Interface resistance plays an important role in the electrochemical performance of ASSLBs. Yu et al. assembled the S-C/ $\text{Li}_6\text{PS}_5\text{Cl}/\text{Li}-\text{In}$  ASSLB.<sup>[43c]</sup> After the initial activation cycle, the discharge capacities of the second and third cycles were 1388.5 and  $1459.0 \text{ mAh g}^{-1}$ , respectively, slightly lower than the theoretical capacity ( $1600 \text{ mAh g}^{-1}$ ) of sulfur.<sup>[60]</sup> The capacity of the S-C/ $\text{Li}_6\text{PS}_5\text{Cl}/\text{Li}-\text{In}$  ASSLB decreased rapidly in subsequent cycles to  $389 \text{ mAh g}^{-1}$  after 20 cycles. The electrochemical impedance spectrum shows that the weak recycling capacity of ASSLB is mainly due to the increased interfacial resistance between solid-state electrolyte and cathode mixture during the cycle. Kim et al. reported a scalable fabrication protocol for ASSLB electrodes composed of a conventional composite LIB electrode and a homogeneous SSE solution ( $\text{Li}_6\text{PS}_5\text{Cl}$  in ethanol).<sup>[109]</sup>  $\text{Li}_6\text{PS}_5\text{Cl}$ /ethanol solution penetrates the curved porous structure of LIB electrodes and solidifies, leading to close ionic contact and good ionic permeation. This  $\text{Li}_6\text{PS}_5\text{Cl}$ -permeated  $\text{LiCoO}_2$  and graphite electrodes exhibit high reversible capacities of 141 and  $364 \text{ mAh g}^{-1}$  at  $30^\circ\text{C}$  and  $0.14 \text{ mA cm}^{-2}$ , respectively, which are superior to traditional dry-mixed ASSLB electrodes. ASSLB prepared by  $\text{Li}_6\text{PS}_5\text{Cl}$  permeating  $\text{LiCoO}_2$  and graphite electrodes has good electrochemical properties at  $100^\circ\text{C}$ , which highlights the excellent thermal stability and safety of ASSLBs.

Although lithium argyrodite SSEs have made great progress recently, their unstable defect leads to the unsatisfactory cycle life of ASSLBs. Until now, limited reports about lithium argyrodite-based ASSLBs with long cycle life (more details are seen in Table 3), which were only realized in labs. To realize the commercial application of lithium argyrodite SSEs on large scale, the stability of argyrodites type SSEs may be the main issue that should be solved first.

## 6. Conclusions and Perspective

In this review, the structure, ion transport mechanism, factors affecting ionic conductivity, synthesis methods, stability, interface issues, and their applications of lithium argyrodite SSEs are introduced. Lithium argyrodite has high ionic conductivity ( $>10^{-3} \text{ Scm}^{-1}$ ) at room temperature, which is higher than oxide SSEs and SPEs. The good ductility of argyrodites is conducive to tighter interface contact compared to oxide SSEs, thus a low interface resistance can be realized. Therefore, lithium argyrodite is the most promising SSEs for ASSLBs. In this review, we have drawn the following main conclusions based on the research of lithium argyrodite:

The ionic conductivity of lithium argyrodite is strongly related to its phase structure. Argyrodites are divided into low-

**Table 3.** Batteries with argyrodites as the SSEs.

Electrolyte	Cathode	C-rate or current density	Capacity [mAh g <sup>-1</sup> ]	Number of cycles	T [°C]	Anode
Li <sub>6</sub> PS <sub>5</sub> Br <sup>[107]</sup>	C-LTO/SE (70:30 wt%)	200 μA cm <sup>-2</sup> (C/10)	130	1	75	Li-Al
Li <sub>6</sub> PS <sub>5</sub> Cl <sup>[43b]</sup>	LTO:CSE (66.5:3.5:30 wt%)	–	57	60	RT	Li
Li <sub>6</sub> PS <sub>5</sub> Cl <sup>[44]</sup>	LTO@LPSCL	8.75 mA g <sup>-1</sup> (0.05 C)	158	250	80	Li
Li <sub>6</sub> PS <sub>5</sub> Cl <sup>[49]</sup>	LCO	C/10	33	9	RT	LTO
Li <sub>6</sub> PS <sub>5</sub> Cl <sup>[51]</sup>	LCO	66 μA cm <sup>-2</sup> (C/10)	90	25	RT	Li-In
Li <sub>6</sub> PS <sub>5</sub> Cl <sup>[51]</sup>	LMO	66 μA cm <sup>-2</sup> (C/10)	40	22	RT	Li-In
HT-Li <sub>4.1</sub> Al <sub>0.9</sub> Si <sub>0.9</sub> S <sub>4</sub> <sup>[36a]</sup>	LiNbO <sub>3</sub> -coated LCO	6.85 mA g <sup>-1</sup> (0.05 C)	120	2	25	Li-In
Li <sub>6</sub> PS <sub>5</sub> Br <sup>[55a]</sup>	CuS	11.2 mA g <sup>-1</sup> (C/50)	90	20	RT	In-Li
Li <sub>6</sub> PS <sub>5</sub> Br <sup>[55b]</sup>	Cu-Li <sub>2</sub> S	50 mA g <sup>-1</sup> (0.1 C)	70	20	RT	In
Li <sub>6</sub> PS <sub>5</sub> Br <sup>[108]</sup>	S	167 mA g <sup>-1</sup> (C/10)	1080	50	RT	In-Li
Li <sub>6</sub> PS <sub>5</sub> Br <sup>[86]</sup>	MoS <sub>2</sub>	67 mA g <sup>-1</sup> (C/10)	190	40	RT	In-Li
Li <sub>6</sub> PS <sub>5</sub> Cl <sup>[43c]</sup>	S-C/SE	0.064 mA cm <sup>-2</sup>	389	20	RT	Li-In
Li <sub>6</sub> PS <sub>5</sub> Cl <sup>[51]</sup>	NMC	66 μA cm <sup>-2</sup> (C/10)	60	20	RT	Li-In
Li <sub>6</sub> PS <sub>5</sub> Cl <sup>[109]</sup>	SE-infiltrated LCO	0.14 mA cm <sup>-2</sup> (0.1 C)	141	79	30	Graphite
Li <sub>6</sub> PS <sub>5</sub> Br <sup>[92]</sup>	Li <sub>2</sub> S/SE (wt 1:1)	0.064 mA cm <sup>-2</sup>	628	2	RT	In
Li <sub>6</sub> PS <sub>5</sub> Br <sup>[119]</sup>	Nano-Li <sub>2</sub> S	0.064 mA cm <sup>-2</sup>	500	25	RT	In
Li <sub>6</sub> PS <sub>5</sub> Br <sup>[66]</sup>	NMC:SE:VGCF	0.13 mA cm <sup>-2</sup>	87	10	RT	In
Li <sub>6</sub> PS <sub>5</sub> Cl <sup>[114]</sup>	NCM-622	7.2 mA g <sup>-1</sup> (0.04 C)	172.8	1	RT	In
Li <sub>6</sub> , <sub>0.4</sub> Ge <sub>0.6</sub> S <sub>5</sub> <sup>[33c]</sup>	NCM-622	0.25 C	99.3	50	60	LTO
Li <sub>6</sub> PS <sub>5</sub> Cl <sup>[120]</sup>	S	C/2	580	50	RT	Li
Li <sub>6</sub> PS <sub>5</sub> Br <sup>[120]</sup>	S	C/2	>900	5	RT	Li
Li <sub>6</sub> PS <sub>5</sub> Cl <sup>[9]</sup>	S/MWCNT/SE	0.176 mA cm <sup>-2</sup> (0.1 C)	1393	50	RT	Li-In
Li <sub>6</sub> PS <sub>5</sub> Cl <sup>[56]</sup>	80Li <sub>2</sub> S-20Li <sub>1</sub>	0.128 mA cm <sup>-2</sup>	330.0	40	RT	In
Li <sub>6</sub> PS <sub>5</sub> Cl <sup>[96]</sup>	NCM-811/C/EC	10 mA g <sup>-1</sup> (0.05 C)	100.2	100	30	Li
Li <sub>6</sub> PS <sub>5</sub> Cl <sup>[38]</sup>	SE-coated MoS <sub>2</sub>	0.13 mA cm <sup>-2</sup>	374	2	RT	In-Li
Li <sub>6</sub> PS <sub>5</sub> Cl <sup>[61]</sup>	NCM-622	2 C	62	25	RT	Li, <sub>0.5</sub> In
Li <sub>6.25</sub> PS <sub>5.25</sub> Cl <sub>0.75</sub> /PEO <sup>[98c]</sup>	LiFePO <sub>4</sub> /Super-P/PVDF	0.2 C	141.8	100	60	Li
Li <sub>6</sub> PS <sub>5</sub> Cl <sup>[83c]</sup>	LiNbO <sub>3</sub> -coated NCM622	18 mA g <sup>-1</sup> (C/10)	150	20	25	LTO
Li <sub>6</sub> PS <sub>5</sub> Cl <sup>[88]</sup>	Li <sub>6</sub> PS <sub>5</sub> Cl-MWCNT	48 mA g <sup>-1</sup>	516	100	RT	Li-In
Li <sub>6</sub> PS <sub>5</sub> Br <sup>[60]</sup>	C-Li <sub>6</sub> PS <sub>5</sub> Br	0.13 mA cm <sup>-2</sup>	157.03	35	RT	Li-In
Li <sub>6</sub> PS <sub>5</sub> Cl / (5 wt%)PEO <sup>[100c]</sup>	NCM-811	0.3 mA cm <sup>-2</sup>	75.6	200	30	Li
Li <sub>2.25</sub> Si <sub>0.25</sub> P <sub>0.75</sub> S <sub>6</sub> <sup>[121]</sup>	TiS <sub>2</sub>	0.1 C	150	10	RT	Li
Li <sub>6</sub> PS <sub>4.7</sub> O <sub>0.3</sub> Br <sup>[122]</sup>	NCM-811	0.8 C	47.4	92	RT	Li-In
Li <sub>5.5</sub> PS <sub>4.5</sub> Cl <sub>1.5</sub> <sup>[8b]</sup>	LiNbO <sub>3</sub> coated NCM-622	0.2 C	135.7	6	25	Li-In
PI-Li <sub>6</sub> PS <sub>5</sub> Cl <sub>0.5</sub> Br <sub>0.5</sub> <sup>[103]</sup>	NCM-622	0.1 C	125.56	100	30	Graphite
Li <sub>6</sub> PS <sub>5</sub> Cl <sup>[110]</sup>	LiNi <sub>0.90</sub> Co <sub>0.05</sub> Mn <sub>0.05</sub> O <sub>2</sub> @LZO	3.4 mA cm <sup>-2</sup> (0.5 C)	129.94	1000	RT	Ag-C
Li <sub>6</sub> PS <sub>5</sub> Cl @wood <sup>[75]</sup>	LTO	0.2 C	123	20	RT	Li
Li <sub>5.5</sub> PS <sub>4.5</sub> Br <sub>1.5</sub> <sup>[83b]</sup>	LiNbO <sub>3</sub> -coated NCM-622	0.255 mA cm <sup>-2</sup> (~0.2 C)	98.4	45	RT	In
Li <sub>5.7</sub> PS <sub>4.5</sub> Cl <sub>1.3</sub> <sup>[80b]</sup>	LiNbO <sub>3</sub> -coated NCM811	0.382 mA cm <sup>-2</sup>	121.7	2	RT	In
Li <sub>5.5</sub> PS <sub>4.5</sub> Cl <sub>1.5</sub> <sup>-</sup> Li <sub>9.54</sub> Si <sub>1.74</sub> <sup>-</sup> (P <sub>0.9</sub> Sb <sub>0.1</sub> ) <sub>1.44</sub> S <sub>11.7</sub> Cl <sub>0.3</sub> -Li <sub>5.5</sub> PS <sub>4.5</sub> Cl <sub>1.5</sub> <sup>[11]</sup>	NMC811	8.6 mA cm <sup>-2</sup> (20 C)	81.0	1	55	Li-Graphite

LTO: Li<sub>4</sub>Ti<sub>5</sub>O<sub>12</sub>; LCO: LiCoO<sub>2</sub>; LMO: LiMn<sub>2</sub>O<sub>4</sub>; NMC: LiNi<sub>1/3</sub>Co<sub>1/3</sub>Mn<sub>1/3</sub>O<sub>2</sub>; NCM-622: LiNi<sub>0.6</sub>Co<sub>0.2</sub>Mn<sub>0.2</sub>O<sub>2</sub>; NCM-811: LiNi<sub>0.8</sub>Co<sub>0.1</sub>Mn<sub>0.1</sub>O<sub>2</sub>; VGCF: vapor grown carbon fiber; MWCNT: multiwall carbon nanotube; EC: ethyl cellulose; SE: solid electrolyte; RT: room temperature.

temperature phases and high-temperature phases. The space group of low-temperature phase argyrodites is Pna2<sub>1</sub>, while the high-temperature phase space group is F43m. More studies have been carried out on the high-temperature phase of argyrodites due to their high ionic conductivity. The transport path of Li<sup>+</sup> in high-temperature phase argyrodites can be divided into three jump types, which are recorded as doublet transition (48 h-24 g-48 h), intra-cage transition (48 h-48 h), and inter-cage transition (48 h-48 h). The disordered distribution of halogens at the 4c and 4d sites has a significant influence on ionic conductivity. By controlling the sintering temperature or introducing halogens, the degree of disorder of halogens becomes manageable, thereby improving the ionic conductivity of lithium argyrodite.

Synthetic methods play the important role in determining the Li<sup>+</sup> conductivity of lithium argyrodite SSEs. At present, there are two main synthetic methods for argyrodites including solid-state synthesis and wet chemical method. Solid-state

synthesis is time-consuming, but the ionic conductivity of SSEs is relatively high, which is ascribed to the less impurity content in argyrodites. During the solid-state synthesis method, the subsequent sintering process is necessary, and the sintering parameters play a direct role in the crystallinity of argyrodites. Rapid heat treatment and cooling are conducive to improving the high ionic conductivity of lithium argyrodite. The wet chemical method is usually used to coat lithium argyrodite on active electrode materials to increase a large contact area, thus decreasing the interfacial resistance. However, it is difficult to remove the solvent in the followed process, resulting in the low ionic conductivity of lithium argyrodite.

Lithium argyrodite is instability at high temperatures, thus the synthesized temperature should be optimized. Cogent studies showed that the optimal sintering temperature is 550 °C. Theoretically, argyrodites are unstable in the air. Lithium argyrodite can be exposed to the air for a short time, and the ionic conductivity of lithium argyrodite does not significantly

decrease, which avails for further application in commercial ASSLBs. Lithium argyrodite is thermodynamically unstable to lithium, but the passivation layer can be formed due to the decomposition reaction that occurred between Li and lithium argyrodite. As a result, lithium can be directly served as a negative electrode to some extent. The slow kinetics of decomposition and the indirect decomposition mechanism caused by de/lithiation lead to a wide electrochemical window of lithium argyrodite as confirmed by CV characterizations. From the point of view of applications, the stability of lithium argyrodite in humid air is still needed to be improved to reduce the processing steps and costs.

When lithium argyrodite is mixed with a typical oxide material for cathodic electrodes, a space charge layer will be formed between argyrodites and oxide positive electrodes. The surface phase structure of lithium argyrodite would be changed, which is detrimental to ionic conductivity. The introduction of oxygen into the electrolyte inhibits the formation of a space charge layer, thus stabilizing the interface. In addition, the use of a conductive agent with a smaller specific surface area can reduce the redox reaction of argyrodites. For the anode, the issue from the interface between argyrodites and Li can be solved by introducing oxygen, lithium halide, or using a thin intermediate layer. The uneven deposition of lithium at the interface can lead to the formation of Li-dendrites. Through surface modification or introducing a special solid electrolyte structure, lithium can be uniformly deposited at the interface, thus inhibiting the growth of Li-dendrites.

Overall, productive results have been reported for the development of lithium argyrodite electrolytes with respect to ionic conductivity chemical and electrochemical stabilities, and techniques for assembling ASSLBs. Whereas there are still big challenges to be overcome for further practical applications. Some important issues for future directions for further developments of lithium argyrodite electrolytes for high-performance ASSLBs are proposed. Firstly, in view of the low-quality, high-energy consumption, and time-consuming for mechanical milling and solid-state reactions as well as the poor ionic conductivity of produced lithium argyrodite, improvements of present-existing techniques or a new synthesis route for lithium argyrodite with low cost, high quality, and scalability are very important for accelerating the application of ASSLBs. Secondly, enhancing the ionic conductivity of cold-pressed lithium argyrodite through optimization of synthesis parameters, tailoring the degree of halogens disorder, and partial substitution of the components is useful for improving the rate capabilities and reducing the polarization for the ASSLBs. Thirdly, uncovering the structural evolution and hydrolysis mechanism of lithium argyrodite exposed in water and air and unraveling the interfaces including the anode materials/lithium argyrodite and cathodes/lithium argyrodite may provide valuable guidance for developing new-type lithium argyrodite with good compatibility and anti-water/air properties for reducing the manufacturing costs and improving the cyclability of ASSLBs. Lastly, innovating conceit and technical experimental study on assembling the lithium argyrodite-based ASSLBs

should be proposed and put into practice, which is vital for future commercial application.

## Acknowledgements

This work was supported by National Natural Science Foundation of China (No. 51902188), Natural Science Foundation of Jiangsu Province (No. BK20190207), Natural Science Doctoral Foundation of Shandong Province (No. ZR2019BEM019), the Future Program for Young Scholar of Shandong University.

## Conflict of Interest

The authors declare no conflict of interest.

**Keywords:** ionic conductivity · lithium argyrodite · lithium metal · solid-state batteries · solid-state electrolyte

- [1] Q. Zhao, S. Stalin, C.-Z. Zhao, L. A. Archer, *Nat. Rev. Mater.* **2020**, *5*, 229.
- [2] Y. Shen, Y. Zhang, S. Han, J. Wang, Z. Peng, L. Chen, *Joule* **2018**, *2*, 1674.
- [3] F. Han, A. S. Westover, J. Yue, X. Fan, F. Wang, M. Chi, D. N. Leonard, N. J. Dudney, H. Wang, C. Wang, *Nat. Energy* **2019**, *4*, 187.
- [4] a) F. Hippauf, B. Schumm, S. Doerfler, H. Althues, S. Fujiki, T. Shiratsuchi, T. Tsujimura, Y. Aihara, S. Kaskel, *Energy Storage Mater.* **2019**, *21*, 390; b) G. F. Dewald, Z. Liaqat, M. A. Lange, W. Tremel, W. Zeier, *Angew. Chem. Int. Ed. Engl.* **2021**, *60*, 17952; c) C. Hänsel, D. Kundu, *Adv. Mater. Interfaces* **2021**, *8*, 2100206; d) J. Y. Kim, J. Park, S. H. Kang, S. Jung, D. O. Shin, M. J. Lee, J. Oh, K. M. Kim, J. Zausch, Y.-G. Lee, Y. M. Lee, *Energy Storage Mater.* **2021**, *41*, 289; e) K. T. Kim, D. Y. Oh, S. Jun, Y. B. Song, T. Y. Kwon, Y. Han, Y. S. Jung, *Adv. Energy Mater.* **2021**, *11*; f) P. Minnemann, L. Quillman, S. Burkhardt, F. H. Richter, J. Janek, *J. Electrochem. Soc.* **2021**, 168.
- [5] a) B. J. Morgan, *Chem. Mater.* **2021**, *33*, 3004; b) S. Wang, W. Zhang, X. Chen, D. Das, R. Ruess, A. Gautam, F. Walther, S. Ohno, R. Koerver, Q. Zhang, W. G. Zeier, F. H. Richter, C. W. Nan, J. Janek, *Adv. Energy Mater.* **2021**, *11*; c) Y. Wang, J. Ju, S. Dong, Y. Yan, F. Jiang, L. Cui, Q. Wang, X. Han, G. Cui, *Adv. Funct. Mater.* **2021**, 31.
- [6] a) J. Zhang, Z. Chen, Q. Ai, T. Terlier, F. Hao, Y. Liang, H. Guo, J. Lou, Y. Yao, *Joule* **2021**, *5*, 1845; b) C. Zheng, J. Zhang, Y. Xia, H. Huang, Y. Gan, C. Liang, X. He, X. Tao, W. Zhang, *Small* **2021**, DOI: 10.1002/smll.202101326e2101326; c) G. L. Zhu, C. Z. Zhao, H. J. Peng, H. Yuan, J. K. Hu, H. X. Nan, Y. Lu, X. Y. Liu, J. Q. Huang, C. He, J. Zhang, Q. Zhang, *Adv. Funct. Mater.* **2021**, 31.
- [7] a) K. Park, B. C. Yu, J. B. Goodenough, *Adv. Energy Mater.* **2016**, *6*, 1502534; b) R. Yu, Q.-X. Du, B.-K. Zou, Z.-Y. Wen, C.-H. Chen, *J. Power Sources* **2016**, *306*, 623; c) Y. Li, Y. Sun, A. Pei, K. Chen, A. Vailionis, Y. Li, G. Zheng, J. Sun, Y. Cui, *ACS Cent. Sci.* **2018**, *4*, 97; d) T. Krauskopf, R. Dippel, H. Hartmann, K. Peppler, B. Mogwitz, F. H. Richter, W. G. Zeier, J. Janek, *Joule* **2019**, *3*, 2030; e) Z. Zhang, Z. Zou, K. Kaup, R. Xiao, S. Shi, M. Avdeev, Y. S. Hu, D. Wang, B. He, H. Li, *Adv. Energy Mater.* **2019**, *9*, 1902373; f) X. Miao, H. Wang, R. Sun, C. Wang, Z. Zhang, Z. Li, L. Yin, *Energy Environ. Sci.* **2020**, *13*, 3780; g) X. Miao, H. Wang, R. Sun, X. Ge, D. Zhao, P. Wang, R. Wang, L. Yin, *Adv. Energy Mater.* **2021**, *11*, 2003469.
- [8] a) S. Chen, D. Xie, G. Liu, J. P. Mwizerwa, Q. Zhang, Y. Zhao, X. Xu, X. Yao, *Energy Storage Mater.* **2018**, *14*, 58; b) W. D. Jung, J. S. Kim, S. Choi, S. Kim, M. Jeon, H. G. Jung, K. Y. Chung, J. H. Lee, B. K. Kim, J. H. Lee, H. Kim, *ACS Appl. Mater. Interfaces* **2020**, *20*, 2303.
- [9] S. Wang, Y. Zhang, X. Zhang, T. Liu, Y. H. Lin, Y. Shen, L. Li, C. W. Nan, *ACS Appl. Mater. Interfaces* **2018**, *10*, 42279.
- [10] Y.-g. Lee, S. Fujiki, C. Jung, N. Suzuki, N. Yashiro, R. Omada, D.-s. Ko, T. Shiratsuchi, T. Sugimoto, S. Ryu, J. H. Ku, T. Watanabe, Y. Park, Y. Aihara, D. Im, I. T. Han, *Nat. Energy* **2020**, *5*, 299.
- [11] L. Ye, X. Li, *Nature* **2021**, *593*, 218.

- [12] H. J. Deiseroth, S. T. Kong, H. Eckert, J. Vannahme, C. Reiner, T. Zaiß, M. Schlosser, *Angew. Chem. Int. Ed.* **2008**, *47*, 755.
- [13] S. T. Kong, Ö. Gün, B. Koch, H. J. Deiseroth, H. Eckert, C. Reiner, *Chem. Eur. J.* **2010**, *16*, 5138.
- [14] C. Wang, K. Fu, S. P. Kammampata, D. W. McOwen, A. J. Samson, L. Zhang, G. T. Hitz, A. M. Nolan, E. D. Wachsman, Y. Mo, V. Thangadurai, L. Hu, *Chem. Rev.* **2020**, *120*, 4257.
- [15] V. Epp, Ö. Gün, H. J. Deiseroth, M. Wilkening, *Phys. Chem. Chem. Phys.* **2013**, *15*, 7123.
- [16] O. Pecher, S. T. Kong, T. Goebel, V. Nickel, K. Weichert, C. Reiner, H. J. Deiseroth, J. Maier, F. Haarmann, D. Zahn, *Chem. Eur. J.* **2010**, *16*, 8347.
- [17] H. J. Deiseroth, J. Maier, K. Weichert, V. Nickel, S. T. Kong, C. Reiner, Z. Anorg. Allg. Chem. **2011**, *637*, 1287.
- [18] a) V. Epp, O. Guen, H.-J. Deiseroth, M. Wilkening, *J. Phys. Chem. Lett.* **2013**, *4*, 2118; b) S. Ganapathy, C. Yu, E. R. H. van Eck, M. Wagemaker, *ACS Energy Lett.* **2019**, *4*, 1092.
- [19] M. Brinek, C. Hiebl, H. M. R. Wilkening, *Chem. Mater.* **2020**, *32*, 4754.
- [20] I. Hanghofer, B. Gadermaier, H. M. R. Wilkening, *Chem. Mater.* **2019**, *31*, 4591.
- [21] A. R. Stamminger, B. Ziebarth, M. Mrovec, T. Hammerschmidt, R. Drautz, *Chem. Mater.* **2019**, *31*, 8673.
- [22] C. Yu, S. Ganapathy, N. J. J. De Klerk, I. Roslon, E. R. H. Van Eck, A. P. M. Kentgens, M. Wagemaker, *J. Am. Chem. Soc.* **2016**, *138*, 11192.
- [23] N. J. J. De Klerk, I. Rosłoń, M. Wagemaker, *Chem. Mater.* **2016**, *28*, 7955.
- [24] a) H. M. Chen, C. Maohua, S. Adams, *Phys. Chem. Chem. Phys.* **2015**, *17*, 16494; b) N. Minafra, M. A. Kraft, T. Bernges, C. Li, R. Schlem, B. J. Morgan, W. G. Zeier, *Inorg. Chem.* **2020**, *59*, 11009.
- [25] Z. Deng, Z. Zhu, I.-H. Chu, S. P. Ong, *Chem. Mater.* **2017**, *29*, 281.
- [26] Z. Zhang, J. Zhang, H. Jia, L. Peng, T. An, J. Xie, *J. Power Sources* **2020**, *450*, 227601.
- [27] S. T. Kong, O. Guen, B. Koch, H. J. Deiseroth, H. Eckert, C. Reiner, *Chem. Eur. J.* **2010**, *16*, 5138.
- [28] M. Xuan, W. Xiao, H. Xu, Y. Shen, Z. Li, S. Zhang, Z. Wang, G. Shao, *J. Mater. Chem. A* **2018**, *6*, 19231.
- [29] R. Schlem, M. Ghidui, S. P. Culver, A. L. Hansen, W. G. Zeier, *ACS Appl. Energ. Mater.* **2020**, *3*, 9.
- [30] a) P. Adeli, J. D. Bazak, K. H. Park, I. Kochetkov, A. Huq, G. R. Goward, L. F. Nazar, *Angew. Chem. Int. Ed.* **2019**, *58*, 8681; b) C. Yu, Y. Li, M. Willans, Y. Zhao, K. R. Adair, F. Zhao, W. Li, S. Deng, J. Liang, M. N. Banis, R. Li, H. Huang, L. Zhang, R. Yang, S. Lu, Y. Huang, X. Sun, *Nano Energy* **2020**, *69*, 104396.
- [31] L. Zhou, K. H. Park, X. Sun, F. Lalère, T. Adermann, P. Hartmann, L. F. Nazar, *ACS Energy Lett.* **2019**, *4*, 265.
- [32] A. Baktash, J. C. Reid, T. Roman, D. J. Searles, *npj Computational Materials* **2020**, *6*, 1.
- [33] a) N. Minafra, S. P. Culver, T. Krauskopf, A. Senyshyn, W. G. Zeier, *J. Mater. Chem. A* **2018**, *6*, 645; b) S. Ohno, B. Helm, T. Fuchs, G. Dewald, M. A. Kraft, S. P. Culver, A. Senyshyn, W. G. Zeier, *Chem. Mater.* **2019**, *31*, 4936; c) M. A. Kraft, S. Ohno, T. Zinkevich, R. Koerver, S. P. Culver, T. Fuchs, A. Senyshyn, S. Indris, B. J. Morgan, W. G. Zeier, *J. Am. Chem. Soc.* **2018**, *140*, 16330; d) L. Zhou, A. Assoud, Q. Zhang, X. Wu, L. F. Nazar, *J. Am. Chem. Soc.* **2019**, *141*, 19002; e) F. Zhao, J. Liang, C. Yu, Q. Sun, X. Li, K. Adair, C. Wang, Y. Zhao, S. Zhang, W. Li, S. Deng, R. Li, Y. Huang, H. Huang, L. Zhang, S. Zhao, S. Lu, X. Sun, *Adv. Energy Mater.* **2020**, *1903422*, 1903422.
- [34] J. Zhang, L. Li, C. Zheng, Y. Xia, Y. Gan, H. Huang, C. Liang, X. He, X. Tao, W. Zhang, *ACS Appl. Mater. Interfaces* **2020**, *12*, 41538.
- [35] Y. B. Song, D. H. Kim, H. Kwak, D. Han, S. Kang, J. H. Lee, S.-M. Bak, K.-W. Nam, H.-W. Lee, Y. S. Jung, *Nano Lett.* **2020**, *20*, 4337.
- [36] a) W. Huang, K. Yoshino, S. Hori, K. Suzuki, M. Yonemura, M. Hirayama, R. Kanno, *J. Solid State Chem.* **2019**, *270*, 487; b) W. Huang, C. LinDong, S. Hori, K. Suzuki, M. Yonemura, M. Hirayama, R. Kanno, *Materials Advances* **2020**, *1*, 334; c) F. Strauss, T. Zinkevich, S. Indris, T. Brezesinski, *Inorg. Chem.* **2020**, *59*, 12954.
- [37] F. Walther, R. Koerver, T. Fuchs, S. Ohno, J. Sann, M. Rohnke, W. G. Zeier, J. Janek, *Chem. Mater.* **2019**, *31*, 3745.
- [38] Z. Zhang, L. Zhang, Y. Liu, C. Yu, X. Yan, B. Xu, L. M. Wang, *J. Alloys Compd.* **2018**, *747*, 227.
- [39] S. Wenzel, S. J. Sedlmaier, C. Dietrich, W. G. Zeier, J. Janek, *Solid State Ionics* **2018**, *318*, 102.
- [40] S. H. Kim, K. Kim, H. Choi, D. Im, S. Heo, H. S. Choi, *J. Mater. Chem. A* **2019**, *7*, 13650.
- [41] J. M. Doux, H. Nguyen, D. H. S. Tan, A. Banerjee, X. Wang, E. A. Wu, C. Jo, H. Yang, Y. S. Meng, *Adv. Energy Mater.* **2020**, *10*, 1903253.
- [42] J. B. Goodenough, Y. Kim, *Chem. Mater.* **2010**, *22*, 587.
- [43] a) R. P. Rao, S. Adams, *Phys. Status Solidi A* **2011**, *208*, 1804; b) R. P. Rao, N. Sharma, V. K. Peterson, S. Adams, *Solid State Ionics* **2013**, *230*, 72; c) C. Yu, L. van Eijck, S. Ganapathy, M. Wagemaker, *Electrochim. Acta* **2016**, *215*, 93.
- [44] A. Hwang, Y. Ma, Y. Cao, Q. Li, L. Wang, X. Cheng, P. Zuo, C. Du, Y. Gao, G. Yin, *Int. J. Electrochem. Sci.* **2017**, *12*, 7795.
- [45] S. Boulineau, M. Courty, J. M. Tarascon, V. Viallet, *Solid State Ionics* **2012**, *221*, 1.
- [46] F. Han, Y. Zhu, X. He, Y. Mo, C. Wang, *Adv. Energy Mater.* **2016**, *6*, 1501590.
- [47] a) T. K. Schwietert, V. A. Arszlewska, C. Wang, C. Yu, A. Vasileiadis, N. J. J. de Klerk, J. Hageman, T. Hupfer, I. Kerkamm, Y. Xu, E. van der Maas, E. M. Kelder, S. Ganapathy, M. Wagemaker, *Nat. Mater.* **2020**, *19*, 428; b) W. D. Richards, L. J. Miara, Y. Wang, J. C. Kim, G. Ceder, *Chem. Mater.* **2015**, *28*, 266; c) Y. Zhu, X. He, Y. Mo, *ACS Appl. Mater. Interfaces* **2015**, *7*, 23685.
- [48] S. Ohno, C. Rosenbach, G. F. Dewald, J. Janek, W. G. Zeier, *Adv. Funct. Mater.* **2021**, *31*.
- [49] J. Auvergniot, A. Cassel, D. Foix, V. Viallet, V. Seznec, R. Dedryvère, *Solid State Ionics* **2017**, *300*, 78.
- [50] S. Boulineau, J. M. Tarascon, J. B. Leriche, V. Viallet, *Solid State Ionics* **2013**, *242*, 45.
- [51] J. Auvergniot, A. Cassel, J. B. Ledeuil, V. Viallet, V. Seznec, R. Dedryvère, *Chem. Mater.* **2017**, *29*, 3883.
- [52] D. H. S. Tan, E. A. Wu, H. Nguyen, Z. Chen, M. A. T. Marple, J. M. Doux, X. Wang, H. Yang, A. Banerjee, Y. S. Meng, *ACS Energy Lett.* **2019**, DOI: 10.1021/acsenergylett.9b016932418.
- [53] S. W. Park, G. Oh, J.-W. Park, Y.-C. Ha, S.-M. Lee, S. Y. Yoon, B. G. Kim, *Small* **2019**, *15*, 1900235.
- [54] F. Strauss, J. H. Teo, A. Schiele, T. Bartsch, T. Hatsuake, P. Hartmann, J. Janek, T. Brezesinski, *ACS Appl. Mater. Interfaces* **2020**, *12*, 20462.
- [55] a) M. Chen, R. Prasada Rao, S. Adams, *Solid State Ionics* **2014**, *268*, 300; b) M. Chen, R. P. Rao, S. Adams, *Solid State Ionics* **2014**, *262*, 183.
- [56] C. Yu, S. Ganapathy, J. Hageman, L. Van Eijck, E. R. H. Van Eck, L. Zhang, T. Schwietert, S. Basak, E. M. Kelder, M. Wagemaker, *ACS Appl. Mater. Interfaces* **2018**, *10*, 33296.
- [57] R. Chen, Q. Li, X. Yu, L. Chen, H. Li, *Chem. Rev.* **2020**, *120*, 6820.
- [58] H. Schneider, H. Du, T. Kelley, K. Leitner, J. ter Maat, C. Scordilis-Kelley, R. Sanchez-Carrera, I. Kovalev, A. Mudalige, J. Kulisch, M. M. Safont-Sempere, P. Hartmann, T. Weiß, L. Schneider, B. Hinrichsen, *J. Power Sources* **2017**, *366*, 151.
- [59] R. P. Rao, S. Adams, *Indonesian Journal of Materials Science* **2010**, *130419*.
- [60] C. Yu, J. Hageman, S. Ganapathy, L. Van Eijck, L. Zhang, K. R. Adair, X. Sun, M. Wagemaker, *J. Mater. Chem. A* **2019**, *7*, 10412.
- [61] A. Gautam, M. Sadowski, N. Prinz, H. Eickhoff, N. Minafra, M. Ghidui, S. P. Culver, K. Albe, T. F. Fässler, M. Zobel, W. G. Zeier, *Chem. Mater.* **2019**, *31*, 10178.
- [62] S. Yubuchi, S. Teragawa, K. Aso, K. Tadanaga, A. Hayashi, M. Tatsumisago, *J. Power Sources* **2015**, *293*, 941.
- [63] S. Yubuchi, M. Uematsu, M. Deguchi, A. Hayashi, M. Tatsumisago, *ACS Appl. Energ. Mater.* **2018**, *1*, 3622.
- [64] a) S. Yubuchi, H. Tsukasaki, A. Sakuda, S. Mori, A. Hayashi, M. Tatsumisago, *RSC Adv.* **2019**, *9*, 14465; b) S. Yubuchi, M. Uematsu, C. Hotehama, A. Sakuda, A. Hayashi, M. Tatsumisago, *J. Mater. Chem. A* **2019**, *7*, 558.
- [65] S. Choi, J. Ann, J. Do, S. Lim, C. Park, D. Shin, *J. Electrochem. Soc.* **2019**, *166*, A5193.
- [66] S. Chida, A. Miura, N. C. Rosero-Navarro, M. Higuchi, N. H. H. Phuc, H. Muto, A. Matsuda, K. Tadanaga, *Ceram. Int.* **2018**, *44*, 742.
- [67] a) H. Ling, L. Shen, Y. Huang, J. Ma, L. Chen, X. Hao, L. Zhao, F. Kang, Y.-B. He, *ACS Appl. Mater. Interfaces* **2020**, *12*, 56995; b) D. Zhou, R. Liu, Y. B. He, F. Li, M. Liu, B. Li, Q. H. Yang, Q. Cai, F. Kang, *Adv. Energy Mater.* **2016**, *6*, 1502214.
- [68] a) X. Wang, W. Zeng, L. Hong, W. Xu, H. Yang, F. Wang, H. Duan, M. Tang, H. Jiang, *Nat. Energy* **2018**, *3*, 227; b) J. Liang, X. Li, Y. Zhao, L. V. Goncharova, W. Li, K. R. Adair, M. N. Banis, Y. Hu, T. K. Sham, H. Huang, L. Zhang, S. Zhao, S. Lu, R. Li, X. Sun, *Adv. Energy Mater.* **2019**, *9*, 1; c) J. Kasemchainan, S. Zekoll, D. Spencer Jolly, Z. Ning, G. O. Hartley, J. Marrow, P. G. Bruce, *Nat. Mater.* **2019**, *18*, 1105; d) Q. Lu, Y. B. He, Q. Yu, B. Li, Y. V. Kaneti, Y. Yao, F. Kang, Q. H. Yang, *Adv. Mater.* **2017**, *29*, 1604460; e) S. Li, S. Q. Zhang, L. Shen, Q. Liu, J. B. Ma, W. Lv, Y. B. He, Q. H. Yang, *Adv. Sci.* **2020**, *7*, 1903088.
- [69] Z. Wan, D. Lei, W. Yang, C. Liu, K. Shi, X. Hao, L. Shen, W. Lv, B. Li, Q. H. Yang, *Adv. Funct. Mater.* **2019**, *29*, 1805301.

- [70] F. J. Simon, M. Hanauer, A. Henss, F. H. Richter, J. Janek, *ACS Appl. Mater. Interfaces* **2019**, *11*, 42186.
- [71] F. Zhao, Q. Sun, C. Yu, S. Zhang, K. Adair, S. Wang, Y. Liu, Y. Zhao, J. Liang, C. Wang, X. Li, X. Li, W. Xia, R. Li, H. Huang, L. Zhang, S. Zhao, S. Lu, X. Sun, *ACS Energy Lett.* **2020**, *5*, 1035.
- [72] Y. Li, W. Arnold, J. B. Jasinski, A. Thapa, G. Sumanasekera, M. Sunkara, B. Narayanan, T. Druffel, H. Wang, *Electrochim. Acta* **2020**, *363*.
- [73] B. Chen, C. Xu, H. Wang, J. Zhou, *Curr. Appl. Phys.* **2019**, *19*, 149.
- [74] A. Sharafi, H. M. Meyer, J. Nanda, J. Wolfenstein, J. Sakamoto, *J. Power Sources* **2016**, *302*, 135.
- [75] Y. Li, D. Cao, W. Arnold, Y. Ren, C. Liu, J. B. Jasinski, T. Druffel, Y. Cao, H. Zhu, H. Wang, *Energy Storage Mater.* **2020**, *31*, 344.
- [76] J. B. Cook, H. S. Kim, T. C. Lin, S. Robbenbott, E. Detsi, B. S. Dunn, S. H. Tolbert, *ACS Appl. Mater. Interfaces* **2017**, *9*, 19063.
- [77] a) J. Sakabe, N. Ohta, T. Ohnishi, K. Mitsuishi, K. Takada, *Commun. Chem.* **2018**, *1*, 1; b) D. H. Kim, H. A. Lee, Y. B. Song, J. W. Park, S. M. Lee, Y. S. Jung, *J. Power Sources* **2019**, *426*, 143; c) C. Cao, I. I. Abate, E. Sivonxay, B. Shyam, C. Jia, B. Moritz, T. P. Devereaux, K. A. Persson, H. G. Steinrück, M. F. Toney, *Joule* **2019**, *3*, 762.
- [78] S. Cangaz, F. Hippauf, F. S. Reuter, S. Doerfler, T. Abendroth, H. Althues, S. Kaskel, *Adv. Energy Mater.* **2020**, *10*, 2001320.
- [79] S. Yubuchi, W. Nakamura, T. Bibienne, S. Rousset, L. W. Taylor, M. Pasquali, M. Dolle, A. Sakuda, A. Hayashi, M. Tatsumisago, *J. Power Sources* **2019**, *417*, 125.
- [80] Z. Zhang, L. Zhang, Y. Liu, X. Yan, B. Xu, L. M. Wang, *J. Alloys Compd.* **2020**, *812*, 152103.
- [81] J. Zhang, C. Zheng, L. Li, Y. Xia, H. Huang, Y. Gan, C. Liang, X. He, X. Tao, W. Zhang, *Adv. Energy Mater.* **2020**, *10*, 1.
- [82] L. Wang, R. Xie, B. Chen, X. Yu, J. Ma, C. Li, Z. Hu, X. Sun, C. Xu, S. Dong, T. S. Chan, J. Luo, G. Cui, L. Chen, *Nat. Commun.* **2020**, *11*, 5889.
- [83] a) S. H. Jung, K. Oh, Y. J. Nam, D. Y. Oh, P. Bruener, K. Kang, Y. S. Jung, *Chem. Mater.* **2018**, *30*, 8190; b) C. Yu, Y. Li, W. Li, K. R. Adair, F. Zhao, M. Willans, J. Liang, Y. Zhao, C. Wang, S. Deng, R. Li, H. Huang, S. Lu, T.-k. Sham, Y. Huang, X. Sun, *Energy Storage Mater.* **2020**, *30*, 238; c) F. Strauss, D. Stepien, J. Maibach, L. Pfaffmann, S. Indris, P. Hartmann, T. Brezesinski, *RSC Adv.* **2019**, *10*, 1114.
- [84] a) Y. Kato, S. Hori, T. Saito, K. Suzuki, M. Hirayama, A. Mitsui, M. Yonemura, H. Iba, R. Kanno, *Nat. Energy* **2016**, *1*, 1; b) K. H. Park, Q. Bai, D. H. Kim, D. Y. Oh, Y. Zhu, Y. Mo, Y. S. Jung, *Adv. Energy Mater.* **2018**, *8*, 1.
- [85] Y. Jiao, A. M. Hafez, D. Cao, A. Mukhopadhyay, Y. Ma, H. Zhu, *Small* **2018**, *14*, 1800640.
- [86] M. Chen, X. Yin, M. V. Reddy, S. Adams, *J. Mater. Chem. A* **2015**, *3*, 10698.
- [87] S. Ohno, R. Koerver, G. Dewald, C. Rosenbach, P. Titscher, D. Steckermeier, A. Kwade, J. Janek, W. G. Zeier, *Chem. Mater.* **2019**, *31*, 2930.
- [88] S. Wang, X. Xu, X. Zhang, C. Xin, B. Xu, L. Li, Y. H. Lin, Y. Shen, B. Li, C. W. Nan, *J. Mater. Chem. A* **2019**, *7*, 18612.
- [89] Y. Yang, G. Zheng, S. Misra, J. Nelson, M. F. Toney, Y. Cui, *J. Am. Chem. Soc.* **2012**, *134*, 15387.
- [90] H. Wang, C. Yu, S. Ganapathy, E. R. H. van Eck, L. van Eijck, M. Wagemaker, *J. Power Sources* **2019**, *412*, 29.
- [91] K. Shi, Z. Wan, L. Yang, Y. Zhang, Y. Huang, S. Su, H. Xia, K. Jiang, L. Shen, Y. Hu, *Angew. Chem.* **2020**, *132*, 11882.
- [92] C. Yu, S. Ganapathy, E. R. H. V. Eck, H. Wang, S. Basak, Z. Li, M. Wagemaker, *Nat. Commun.* **2017**, *8*, 1.
- [93] F. Han, J. Yue, X. Fan, T. Gao, C. Luo, Z. Ma, L. Suo, C. Wang, *Nano Lett.* **2016**, *16*, 4521.
- [94] D. Y. Oh, K. T. Kim, S. H. Jung, D. H. Kim, S. Jun, S. Jeoung, H. R. Moon, Y. S. Jung, *Mater. Today* **2021**, DOI: 10.1016/j.mattod.2021.01.006.
- [95] N. C. Rosero-Navarro, T. Kinoshita, A. Miura, M. Higuchi, K. Tadanaga, *Ionics* **2017**, *23*, 1619.
- [96] J. Zhang, H. Zhong, C. Zheng, Y. Xia, C. Liang, H. Huang, Y. Gan, X. Tao, W. Zhang, *J. Power Sources* **2018**, *391*, 73.
- [97] K. Lee, J. Lee, S. Choi, K. Char, J. W. Choi, *ACS Energy Lett.* **2019**, *4*, 94.
- [98] a) M. Ghidiu, J. Ruhl, S. P. Culver, W. G. Zeier, *J. Mater. Chem. A* **2019**, *7*, 17735; b) W. Liu, S. W. Lee, D. Lin, F. Shi, S. Wang, A. D. Sendek, Y. Cui, *Nat. Energy* **2017**, *2*, 1; c) D. Li, L. Cao, C. Liu, G. Cao, J. Hu, J. Chen, G. Shao, *Appl. Surf. Sci.* **2019**, *493*, 1326.
- [99] Q. Zhang, K. Liu, F. Ding, X. Liu, *Nano Res.* **2017**, *10*, 4139.
- [100] a) D. Li, L. Chen, T. Wang, L.-Z. Fan, *ACS Appl. Mater. Interfaces* **2018**, *10*, 7069; b) H. Zhai, P. Xu, M. Ning, Q. Cheng, J. Mandal, Y. Yang, *Nano Lett.* **2017**, *17*, 3182; c) J. Zhang, C. Zheng, J. Lou, Y. Xia, C. Liang, H. Huang, Y. Gan, X. Tao, W. Zhang, *J. Power Sources* **2019**, *412*, 78; d) F. J. Simon, M. Hanauer, F. H. Richter, J. Janek, *ACS Appl. Mater. Interfaces* **2020**, *12*, 11713.
- [101] J. M. Whiteley, P. Taynton, W. Zhang, S. H. Lee, *Adv. Mater.* **2015**, *27*, 6922.
- [102] Y. J. Nam, S.-J. Cho, D. Y. Oh, J.-M. Lim, S. Y. Kim, J. H. Song, Y.-G. Lee, S.-Y. Lee, Y. S. Jung, *Nano Lett.* **2015**, *15*, 3317.
- [103] D. H. Kim, Y. H. Lee, Y. B. Song, H. Kwak, S. Y. Lee, Y. S. Jung, *ACS Energy Lett.* **2020**, *5*, 718.
- [104] S. Wang, X. Zhang, S. Liu, C. Xin, C. Xue, F. Richter, L. Li, L. Fan, Y. Lin, Y. Shen, J. Janek, C. W. Nan, *J. Mater.* **2020**, *6*, 70.
- [105] Z. Zhang, L. Wu, D. Zhou, W. Weng, X. Yao, *Nano Lett.* **2021**, *21*, 5233.
- [106] G. Liu, J. Shi, M. Zhu, W. Weng, L. Shen, J. Yang, X. Yao, *Energy Storage Mater.* **2021**, *38*, 249.
- [107] F. Stadler, C. Fietzek, *ECS Trans.* **2010**, *25*, 177.
- [108] M. Chen, S. Adams, *J. Solid State Electrochem.* **2015**, *19*, 697.
- [109] D. H. Kim, D. Y. Oh, K. H. Park, Y. E. Choi, Y. J. Nam, H. A. Lee, S. M. Lee, Y. S. Jung, *Nano Lett.* **2017**, *17*, 3013.
- [110] X. Shen, C.-C. Yang, Y. Liu, G. Wang, H. Tan, Y.-H. Tung, G. Wang, X. Lu, J. He, X. Zhou, *ACS Appl. Mater. Interfaces* **2019**, *11*, 2168.
- [111] M. A. Kraft, S. P. Culver, M. Calderon, F. Böcher, T. Krauskopf, A. Senyshyn, C. Dietrich, A. Zevalkink, J. Janek, W. G. Zeier, *J. Am. Chem. Soc.* **2017**, *139*, 10909.
- [112] S. T. Kong, H. J. Deiseroth, C. Reiner, Ö. Gün, E. Neumann, C. Ritter, D. Zahn, *Chem. Eur. J.* **2010**, *16*, 2198.
- [113] S. Kalnaus, A. S. Sabau, W. E. Tenhaeff, N. J. Dudney, C. Daniel, *J. Power Sources* **2012**, *201*, 280.
- [114] S. Choi, M. Jeon, B. K. Kim, B. I. Sang, H. Kim, *Chem. Commun.* **2018**, *54*, 14116.
- [115] W. Arnold, D. A. Buchberger, Y. Li, M. Sunkara, T. Druffel, H. Wang, *J. Power Sources* **2020**, *464*, 228158.
- [116] N. C. Rosero-Navarro, A. Miura, K. Tadanaga, *J. Sol-Gel Sci. Technol.* **2019**, *89*, 303.
- [117] M. Duchardt, M. Diels, B. Roling, S. Dehnen, *ACS Appl. Energ. Mater.* **2020**, *3*, 6937.
- [118] D. A. Ziolkowska, W. Arnold, T. Druffel, M. Sunkara, H. Wang, *ACS Appl. Mater. Interfaces* **2019**, *11*, 6015.
- [119] C. Yu, S. Ganapathy, E. R. H. Van Eck, L. Van Eijck, S. Basak, Y. Liu, L. Zhang, H. W. Zandbergen, M. Wagemaker, *J. Mater. Chem. A* **2017**, *5*, 21178.
- [120] R. Prasada Rao, S. Adams, *Solid State Ionics* **2018**, *323*, 97.
- [121] Z. Zhang, Y. Sun, X. Duan, L. Peng, H. Jia, Y. Zhang, B. Shan, J. Xie, *J. Mater. Chem. A* **2019**, *7*, 2717.
- [122] Z. Zhang, L. Zhang, X. Yan, H. Wang, Y. Liu, C. Yu, X. Cao, L. van Eijck, B. Wen, *J. Power Sources* **2019**, *410–411*, 162.

Manuscript received: October 7, 2021

Revised manuscript received: November 14, 2021

Accepted manuscript online: November 17, 2021

Version of record online: December 1, 2021